Project FORTE - Nuclear Thermal Hydraulics Research & Development

Incompressible SPH for Arbitrary Wall Bounded Geometries

August 2019

FNC 53798/48656R Issue 1

FRAZER-NASH CONSULTANCY

SYSTEMS AND ENGINEERING TECHNOLOGY

An introduction to Project FORTE

The Department for Business, Energy and Industrial Strategy (BEIS) has tasked Frazer-Nash Consultancy and its partner organisations to deliver the first phase of a programme of nuclear thermal hydraulics research and development.

Phase 1 of the programme comprises two parts:

- The specification and development of innovative thermal hydraulic modelling methods and tools; and
- The specification of a new United Kingdom thermal hydraulics test facility.

The work is intended to consider all future reactor technologies including Gen III+, small modular reactors and advanced reactor technologies.

Our project partners

The team is led by Frazer-Nash Consultancy and includes:

FRAZER-NASH CONSULTANCY

The University Of Sheffield.

EDF ENERGY

Westinghouse

MANCHESTER 1824 The University of Manchester

Science & Technology Facilities Council

For more information, visit www.innovationfornuclear.co.uk/nuclearthermalhydraulics.html

Executive Summary

The design of Nuclear Power Plants involves complex geometry, such as fuel grid spacers and wire wrapped fuel assemblies. The Finite Difference and Finite Volume CFD modelling techniques that are currently used to resolve the flow, turbulence and heat transfer in these areas require very large meshes that take a significant amount of time to generate and solve.

This report describes novel and original research at the University of Manchester to extend the meshless incompressible Smoothed Particle Hydrodynamics (SPH) scheme to bounded domains, so that it can be applied to arbitrary geometries, as well as multi-phase and multiple continua flows.

This has been achieved through the following innovative SPH developments:

- **Wall bounded arbitrary geometries:** An iterative particle shifting methodology applicable to the Eulerian SPH scheme has been developed where the iterative scheme is only applied once, in the beginning of the simulation as a pre-processing step. The iterative shifting scheme comprises a two-step shifting approach that minimise the particle shifting distance. A polynomial field function of the same order as the kernel with a tolerance over a regular distribution of 10% must also be satisfied before the iteration procedure is considered to have converged. The effectiveness of the iterative shifting scheme for arbitrary wall bounded domains has been demonstrated using a number of 3-D Poiseuille flow test cases in circular and non-circular cross-sections with close to second-order rate of convergence.
- **Higher-order boundary conditions:** A necessity for higher order convergence rates is the use of a higher order wall boundary condition. Therefore, a novel high-order accurate extrapolation technique for the enforcement of wall and open boundaries to high-order accuracy with Eulerian ISPH was developed and validated. Fourth-order convergence was demonstrated for the 3-D spiral annular flow field smoothing kernel interpolations and third-order spatial accuracy was demonstrated for full 3-D simulations of axial flow through a cylindrical annulus.
- **Arbitrary Lagrangian-Eulerian (ALE) formulation:** A consistent ALE SPH scheme was developed in order to attain the Lagrangian characteristics of SPH to make it applicable to multi-phase flows. This ensures near isotropic particle spacing and therefore, near to theoretical convergence rates without an instability developing due to mass flux from the ALE formulation with no corrections needed to increase the accuracy of the SPH discrete operators. The scheme has been validated for unbounded and bounded domains using the Taylor-Green vortices and inviscid vortex test cases, and shows large improvements in accuracy and stability compared to other ALE schemes. A spatial convergence study has also been performed where second- and fourth-order convergence rates have been demonstrated. These developments are directly applicable to, and have been developed to accommodate, interfacial boiling flows.

These innovative SPH developments in terms of accuracy, convergence rates and arbitrary geometries mean that this meshless method could be applied to nuclear thermal hydraulics in realistic geometries. This has the potential to reduce the time and cost associated with nuclear thermal hydraulic analyses in the future.

Contents

1 Introduction

The design of Nuclear Power Plants involves complex geometry, such as fuel grid spacers and wire wrapped fuel assemblies. The Finite Difference and Finite Volume CFD modelling techniques that are currently used to resolve the flow, turbulence and heat transfer in these areas require very large meshes that take a significant amount of time to generate and solve. There are also limitations associated with these schemes especially when dealing with multi-phase and multiple continua, boiling and phase change and in general free surface or interfacial flows. These types of flow exhibit large and non-linear deformations that are difficult to track spatially and temporarily.

To that extent discretisation schemes using meshless computational points have been developed. These new meshless schemes do not require a fixed interconnected mesh to discretise the computational domain and node (or particle) interconnection is calculated using a characteristic length and a weighting function, and usually employ a Lagrangian description of motion. Smoothed Particle Hydrodynamics (SPH) is a new emerging meshless (or mesh-free) discretisation scheme capable of modelling highly non-linear deformations and multiphase flows with complex geometries.

There are a number of SPH variants in computational fluid mechanics such as the strictly incompressible SPH (ISPH) and the weakly compressible SPH scheme. SPH has been extremely successful in a diverse field of science and engineering such as astrophysics [1], environmental flows [2] and lately nuclear decommissioning [3] to name just a few. Nevertheless, SPH has not been applied to nuclear thermal hydraulics with the exception of a few cases [4].

As with most meshless methods, SPH suffers from accuracy artefacts which have deemed the method not appropriate for modelling such flows. Recent studies have shown that modelling turbulence with Large Eddy Simulations (LES) within the SPH scheme, requires a minimum of 30 particles to resolve the smallest eddies in the computational domain. This deems the method computationally expensive [5] and is mainly related to the low order of accuracy of the SPH scheme.

The recent developments of high-order incompressible SPH within an Eulerian framework of Lind and Stansby [6] removed the error associated with non-uniformity of particle distribution, and demonstrated near ideal convergence characteristics with second and higher order convergence rates in unbounded periodic domains. In the nuclear sector, second or higher order convergence rate is essential for thermal hydraulic flows with turbulence and natural or forced convection, especially within an LES modelling framework.

1.1 Objectives

The aim of this work is to extend the incompressible SPH scheme to bounded domains, so that it can be applied to arbitrary geometries, as well as multi-phase and multiple continua flows, which are directly relevant for nuclear thermal hydraulics.

This has been achieved through the following innovative SPH developments:

- **Wall bounded arbitrary geometries:** Section 3 presents the methodology that has been developed to attain second- and high-order characteristics of the Eulerian ISPH scheme for any arbitrary 3-D geometry in a wall bounded domain. The method utilises diffusion-based particle shifting in an iterative manner at the beginning of the simulation to regularize the particle distribution to a near isotropic spacing using a two-step shifting approach. The effectiveness of the iterative procedure is tested using a number of 3-D Poiseuille flow test cases in circular and non-circular cross-sections.

- **Higher-order boundary conditions:** Section 4 details the novel high-order accurate mixed finite difference extrapolation technique that has been developed for wall and open boundary conditions, and shows that the SPH method is capable of higher than second-order accuracy for 3-D flow simulations involving boundaries.
- **Arbitrary Lagrangian-Eulerian (ALE) formulation:** Section 5 discusses the ALE formulation that has been developed with multi-phase flows in mind, where the arbitrary velocity is estimated in such a way that guarantees uniform particle concentration in the domain. Near to theoretical convergence rates provided by the adopted kernel function are achieved ensuring that particle concentration remains uniform during the simulation. The scheme is validated for unbounded and bounded domains using the Taylor-Green vortices and inviscid vortex test cases.

2 SPH Discretisation Scheme

2.1 SPH operators

The SPH operators employed in this work are similar to Xu *et al.* [7] and are as follows. The following form of the gradient operator is used:

$$\nabla\phi_i = -\sum_j^n V_j\left(\phi_i - \phi_j\right)\nabla\omega_{ij} \tag{1}$$

where *i* and *j* is the interpolating particle and its neighbours respectively for a field function ϕ, and *V* is the volume particle. The smoothing kernel W_{ij} is taken to be either the quintic spline [8] with $h = 1.3\Delta x$ or the super-Gaussian [9] fourth order kernel (G4) with $h = 2.0\Delta x$.

The Laplacian operator employed is that suggested by Morris *et al.* [8] and is referred to as the Morris operator henceforth

$$\left(\nabla\cdot\mu\nabla\mathbf{u}\right)_i = \sum_j^n \frac{m_j\left(\mu_i + \mu_j\right)\mathbf{x}_{ij}\cdot\nabla\omega_{ij}}{\rho_j r_{ij}^2}\mathbf{u}_{ij} \tag{2}$$

where **u** is the velocity vector, μ is the dynamic viscosity, *m* and ρ are the mass and density of the particle respectively, and r_{ij} is the magnitude of the distance. The Laplacian operator was chosen with computational efficiency in mind.

2.2 Eulerian ISPH formulation

Similar to the Eulerian ISPH formulation of Lind and Stansby [6], incompressibility is enforced using the projection method of Cummins and Rudman [10] ensuring a divergence-free velocity field. However, the temporal integration scheme is lower than that of Lind and Stansby [6], which is formally second-order.

An intermediate velocity is calculated using a forward Euler scheme, based on the viscous term using the Morris operator and the advection term in the absence of a pressure gradient as

$$\mathbf{u}_i^* = \mathbf{u}_i^n + \left(\nu\nabla^2\mathbf{u}_i^n - \mathbf{u}_i^n\cdot\nabla\mathbf{u}_i^n + \mathbf{g}\right)\Delta t \tag{3}$$

where **g** denotes the external forces such as gravity and the superscript (*) denotes the intermediate step.

The pressure at time *n* + 1 is obtained from the intermediate velocity via solution of the pressure Poisson equation that reads

$$\nabla\cdot\left(\frac{1}{\rho}\nabla p^{n+1}\right)_i = \frac{1}{\Delta t}\nabla\cdot\mathbf{u}_i^* \tag{4}$$

where the Morris operator is used to discretize the left hand side of Equation 4.

Finally, the velocity at time *n* + 1 is obtained by the projection of the intermediate velocity onto the divergence free space,

$$\mathbf{u}_i^{n+1} = \mathbf{u}_i^* - \left(\frac{1}{\rho}\nabla p_i^{n+1}\right)\Delta t \tag{5}$$

Note that, if the particle distribution is regular (uniform), the smoothing error is of *O* (h^2) for the quintic and *O* (h^4) for the G4 kernel as demonstrated by Lind and Stansby [6]. However, in arbitrary bounded domains a regular Cartesian particle distribution is not feasible.

3 SPH for Arbitrary Geometries

The ISPH scheme, based on finding a divergence-free velocity field using a projection method, is known to have noise-free pressures and kinematics for internal and free-surface flows. However, the non-uniformity of particles restricts the accuracy and, consequently, the convergence of the solution to lower than the theoretical second order convergence in smoothing length [11].

The recent developments of high-order incompressible SPH within an Eulerian framework [6] removed the error associated with non-uniformity of particle distribution, and demonstrated near ideal convergence characteristics with second and higher order convergence rates. Conversely, the requirement for uniform particle distributions has thus far restricted the Eulerian scheme to 2-D unbounded or simple rectangular bounded domains [11] with limited applicability to other than idealised test cases. In the nuclear sector, arbitrary geometries are a common occurrence and second or higher order convergence rate is essential for thermal hydraulic flows with turbulence and forced convection, especially within an LES modelling framework.

Regularisation of particle distribution has been an active area of research in SPH. Early, approaches such as XSPH [12] use an additional velocity term based on an SPH interpolation to calculate the particle position. This approach is one of the first particle regularisation approaches to emerge in SPH and has been extensively applied to Weakly Compressible SPH (WCSPH). Since then numerous techniques have been suggested. In the past decade, Xu *et al.* [7] applied a shifting scheme in ISPH based on the geometric distance of neighbouring particles followed by a correction of the hydrodynamic variables.

A similar methodology was used by Lind *et al.* [13] by replacing the geometric shifting criterion with Fick's law of diffusion. The aforementioned particle shifting correction prevented irregular particle distributions by diffusing particles from areas of high concentration to low and vice versa, reducing non-uniformity of particle position. Further, these approaches are applicable to free surface and interfacial flows [13, 14] as shifting is decoupled from the solution of the governing equations and applied only at the end of the time integration step. Additional shifting approaches have emerged lately embedded within an ALE-SPH formulation such as the work of Oger *et al.* [15] or by creating a potential force by using an advection diffusion equation [16]. Further, a remapping of SPH particles to a Cartesian mesh has been proposed by Chaniotis *et al.* [17].

Recently Vacondio and Rogers [18] used a variant of the Fickian shifting of Lind *et al.* [13] in an iterative manner within WCSPH to further improve the spatial accuracy of the SPH gradient calculations using a predefined threshold based on the derivative of the zeroth-order moment. The iterative procedure is applied at each time step if the interpolation error is higher than a pre-defined threshold.

An iterative approach similar to Vacondio and Rogers [18] is proposed in order to attain the second- and high-order characteristics of the Eulerian ISPH for arbitrary 3-D geometries in a bounded domain. The method utilises the diffusion-based particle shifting of Lind *et al.* [13] in an iterative manner at the beginning of the simulation to regularize the particle distribution to a near isotropic spacing. Upon sufficient minimization of the SPH discretisation error, the iterative procedure is terminated and the particle position is fixed in space for the remainder of the simulation. Unlike Vacondio and Rogers [18], the iterative procedure is only applied once for Eulerian SPH, at the beginning of the simulation as pre-processing, and there is no need for the iterative procedure to be applied in the temporal integration.

3.1 Iterative shifting procedure

Lind and Stansby [6] demonstrated that Eulerian SPH offers improvements in accuracy and convergence for a regular isotropic particle distribution arranged in a Cartesian grid by removing the first order error associated with particle anisotropy in a sufficiently smooth kernel near the kernel boundary. However, the applicability of the scheme to 3-D arbitrary wall bounded geometries is not always practical, for instance in domains with curved walls and sharp corners. The wall Boundary Condition (BC) of Adami *et al.* [19] has been used to discretise the arbitrary geometries due to the straightforwardness and flexibility of representing wall BCs, however, this is a lower order method.

3.1.1 Shifting mechanism

Particle regulation schemes improve the accuracy by reducing the spatial anisotropy of particles by a shifting distance of $\delta \mathbf{x}_i$

$$\mathbf{x}_{s,i}^{n+1} = \mathbf{x}_i^{n+1} + \delta \mathbf{x}_i \tag{6}$$

where the subscript *s* denotes the new shifted position. In the diffusion-based scheme [13], the shifting distance is a function of the gradient of the concentration gradient such as

$$\delta \mathbf{x}_i = -Ah^2 \nabla C_i \tag{7}$$

where *A* is a problem dependent constant and taken equal to 0.25 and ∇C_i is simply the derivative of the zeroth moment. By using this procedure at every time step the ∇C_i is reduced, but not necessarily minimised, so that $\delta \mathbf{x}_i \rightarrow 0$. Vacondio and Rogers [18] recognised that by applying the shifting algorithm in an iterative manner could lead to minimisation of the ∇C_i and therefore partially remove the first order error associated with particle anisotropy. Herein, we propose a similar iterative approach based on the diffusion-based scheme [13], where the shifting distance is calculated using Equation 7.

Unlike Vacondio and Rogers [18], the iterative procedure is applied only at the beginning of the simulation in a pre-processing manner since the particle position of the Eulerian particles is fixed in space leading to lower computational cost than the equivalent Lagrangian scheme.

Herein, a two-step shifting procedure is used that involves different kernels to minimise $\delta \mathbf{x}_i$ and the error associated with the derivative of the kernel. Firstly, particles are shifted using Equations 6 and 7 using a lower order kernel. At this step, the aim is to shift particles such that $\delta \mathbf{x}_i \rightarrow 0$. As this is a lower order kernel (different to the kernel used for the interpolations in the time integration), the ∇C_i error with respect to the kernel used in the simulation is large.

For lower order kernels such as the quadratic kernel, the derivative of the kernel function is non-zero at the origin and does not exhibit an extremum in its gradient (while it is discontinuous at its origin). The quadratic kernel in the usual notation reads

$$W(r,h) = a_d \left(\frac{3}{16} q^2 - \frac{3}{4} q + \frac{3}{4} \right) \tag{8}$$

with $\alpha_d = 5/(4\pi h^3)$ in 3-D. Figure 1 shows the quadratic kernel and its derivative.

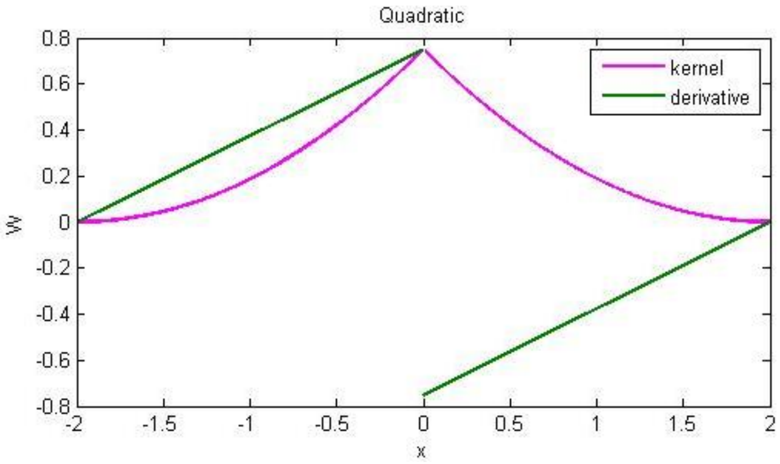

Figure 1: Quadratic smoothing function and its first derivative

As noted by Monaghan [20] and Swegle *et al.* [21] such kernels eliminate the tensile instability which is associated with kernels that exhibit an extremum in their gradient and zero kernel gradient at the origin. In highly random particle domains, the initial particle distribution will exhibit particle clustering within the unstable regime of such kernel derivatives resulting in significant error in the kernel gradient calculation, and thus poor accuracy and convergence of the SPH interpolation. Using the quintic kernel in the diffusion-based scheme particle clumping is eliminated and a near isotropic particle distribution can be recovered as $\delta\mathbf{x}_i \rightarrow 0$. After numerical experiments, it was found that a smoothing length of $h = 1.3\ \Delta x$ is sufficient.

In the second step, the kernel function used for the interpolations in the SPH simulation is used to minimise the ∇C_i. As noted before the quadratic kernel is a lower order kernel and its kernel derivative will exhibit a significant larger error that the quintic and G4 kernels. Therefore, it is necessary to use the diffusion-based shifting to further reduce the kernel gradient error of the near isotropic distribution of “step one” by targeting to minimise ∇C_i in a similar manner to Vacondio and Rogers [18]. Note that in a continuum domain the SPH kernel derivative approximation of a field function *f* can be written as

$$\begin{aligned}\nabla f(\mathbf{x}_i)\big|_{SPH} = {} & f(\mathbf{x}_i)\int_\Omega \nabla W_{ij}\,dx_j + \\ & \nabla f(\mathbf{x}_i)\int_\Omega \left(\mathbf{x}_i-\mathbf{x}_j\right)\frac{\partial W_{ij}}{\partial \mathbf{x}}dx_j + \\ & \frac{1}{2}\nabla^2 f(\mathbf{x}_i)\int_\Omega \left(\mathbf{x}_i-\mathbf{x}_j\right)^2\frac{\partial W_{ij}}{\partial \mathbf{x}}dx_j + \\ & \ldots + O\left(h^n\right)\end{aligned} \tag{9}$$

The first term on the right hand side of Equation 9 is simply the kernel gradient (or ∇C_i), whereas the second and subsequent terms show the error associated with the ability of the kernel derivative to approximate polynomials up to *n* order [22]. Consequently, in order to reduce the SPH interpolation error using an iterative shifting procedure, one must examine both terms with the appropriate kernels.

3.1.2 Convergence of iterative shifting mechanism

In the first step of the iterative shifting procedure, the quadratic kernel shifts particles by a shifting distance of $\delta\mathbf{x}_i$ at each iteration towards an isotropic distribution. As the target of this first step is not the accuracy of the SPH interpolation itself but the distribution of particles in space, a pre-defined threshold can be set to end the first step of the iterative procedure. After numerical experiments, it was found that a maximum threshold of $\delta x_{max} = \max\|\ \delta\mathbf{x}_i\ \|$ of 10^{-6} was sufficiently low for ∇C_i to be approximated with sufficient accuracy for the second step of the algorithm.

Further, it was observed that by setting the threshold of δx_{max} two orders of magnitude higher than the recommended (10^{-4}), there would only be a small number of particles which would have a $\delta \mathbf{x}_i$ near this maximum threshold. This suggests that higher thresholds could be used, which consecutively would reduce the computational cost of the iterative procedure.

The purpose of the second step of the algorithm is to reduce the error of the SPH interpolation. Therefore, one must ensure that a sufficiently low ∇C_i can be achieved. Vacondio and Rogers [18] set a maximum threshold at which the iterative procedure is initiated and suggest that a concentration gradient of the range 10^{-1} to 10^{-2} is sufficient to produce close to second order rate of convergence. This is in line with our findings using a second order accurate kernel (quintic kernel) with a $\delta x_{max} = 10^{-4}$ and an upper concentration gradient of $\nabla C_{max} = 10^{-2}$. Further, in our numerical experiments it was found that a $\nabla C_{max} = 10^{-4}$ is necessary to achieve a convergence rate of the order of three or higher.

Nevertheless, one must also ensure that in Equation 9, the second and following terms also carry a small error. Thus, a test function of order equal to the order of the kernel is used to check the error difference of the regular to shifted particle. In this report, $f(x) = x^2$ and $f(x) = x^4$ is simply used for the quintic and Gaussian G4 respectively. A second threshold of 10% error tolerance from the regular Cartesian particle distribution must also be satisfied for the second step to be terminated in this pre-processing stage and for the SPH simulation to start.

The iterative shifting scheme presented herein has been implemented in the ISPH3D MPI solver capable of running with tens of thousands of processors and simulate hundreds of millions of particles as demonstrated by Guo *et al.* [23].

3.2 Results

In this section, a number of 3-D Poiseuille flow test cases in circular and non-circular cross-sections are presented in order to demonstrate the effectiveness of the iterative shifting procedure. The analytical solutions for viscous flow through pipes of various cross-sections can be found at Bazant [24].

3.2.1 Poiseuille flow in a rectangular channel

A 3-D flow through a square rectangular channel with sides of 1.1 m and length of 5.0 m is simulated with a Reynolds number of $Re = 30$ and dynamic viscosity of $\mu = 10^{-2}$ Pa s. A number of different particle resolutions have been used with $\Delta x = 0.2$, 0.1, 0.05 and 0.025 m to demonstrate the convergence characteristics. Two kernels, the quintic and G4 have been used to simulate the flow through the rectangular channel.

The initial regular particle position is disturbed by a random distance of $0.8\Delta x$ in all directions. A cross-sectional slice of the 3-D domain with $\Delta x = 0.1$ m is shown in Figure 2(a). Note that the wall boundary particles have not been disturbed and are regularly distributed. At the end of the simulation $t = 20.0$ sec, the same cross-sectional slice of the 3-D domain is shown in Figure 2(b) with the 3-D domain shown in Figure 3. These figures demonstrate that the initial random particle distribution has been shifted and a regular Cartesian distribution has been recovered.

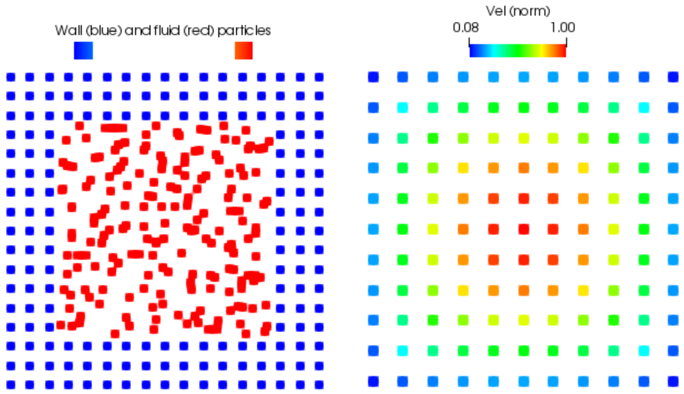

(a) (b)

Figure 2: Cross-sectional slice of the 3-D domain with (a) the initial random particle distribution and (b) fluid particles coloured by normalised velocity of the shifted particle distribution for a rectangular channel with Δx = 0.1 m

To demonstrate the effectiveness of the iterative shifting algorithm for this test case, the shifting and gradient concentration threshold was lowered to 10^{-8}. Figure 4 and Figure 5 show the decay of the $\delta \mathbf{x}_i$ and ∇C_i for the quintic and G4 kernel respectively. Notably, the quintic kernel requires almost three times more iterations to achieve the lower ∇C_i of 10^{-8}, although the kernel support and smoothing size of the G4 is considerably larger. This numerical experiment demonstrates the ability and effectiveness of the high order G4 kernel to deal with near isotropic particle distributions.

Further, the convergence characteristics for the L_2 error norm in velocity is shown in Figure 10 and Figure 11 for the quintic and G4 kernel respectively, with a similar rate of convergence of 1.9. Given the lower order of wall boundary conditions and lower than second order time integration scheme used herein, the rate of convergence is considered satisfactory.

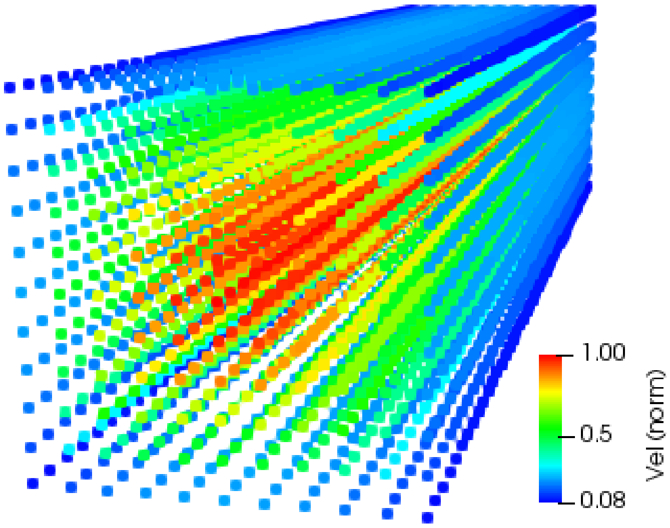

Figure 3: The fluid 3-D domain with the normalised velocity of the shifted particle distribution for a rectangular channel with Δx = 0.1 m

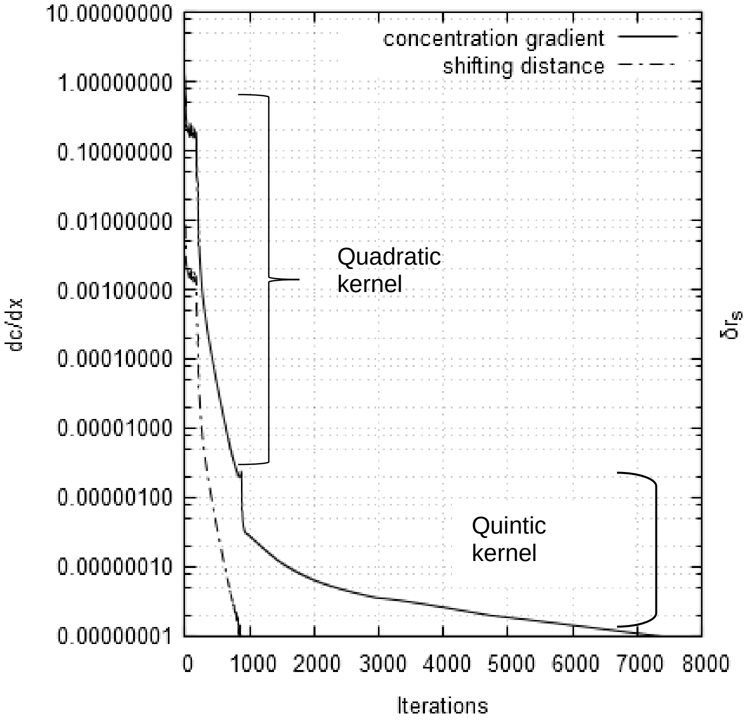

Figure 4: Evolution of particle concentration and shifting distance by the iterative shifting procedure by combining the quadratic and the quintic kernels

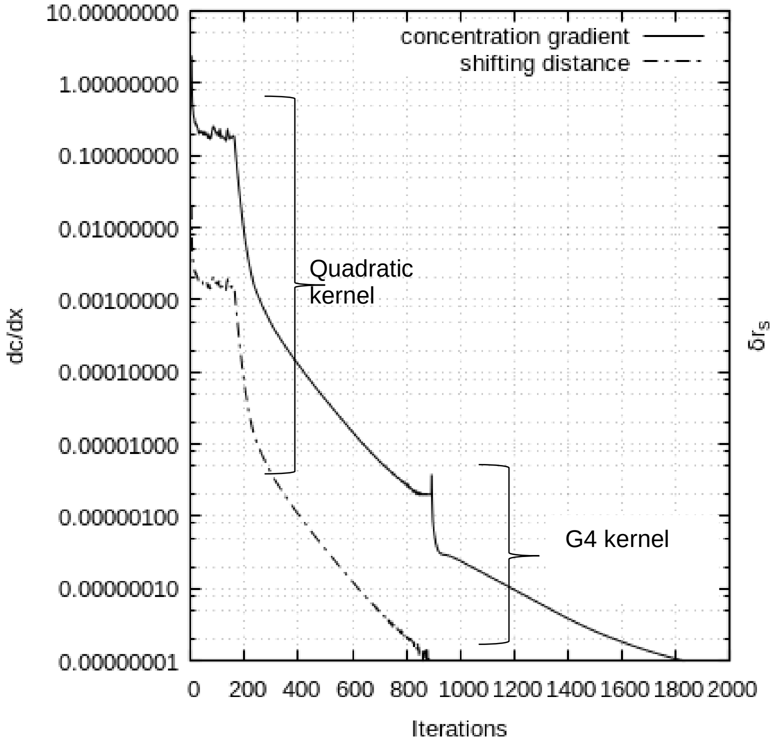

Figure 5: Evolution of particle concentration and shifting distance by the iterative shifting procedure by combining the quadratic and the G4 kernels

3.2.2 Poiseuille flow in an equilateral triangular channel

Similar to the Poiseuille flow in a rectangular channel, an equilateral triangular channel with sides of 1.0 m and length of 5.0 m is simulated with a Reynolds number of $Re = 30$ and dynamic viscosity of $\mu = 10^{-2}$ Pa.s. Three different particle resolutions have been used with $\Delta x = 0.2$, 0.1 and 0.05 m. The quadratic kernel has been used in this test case.

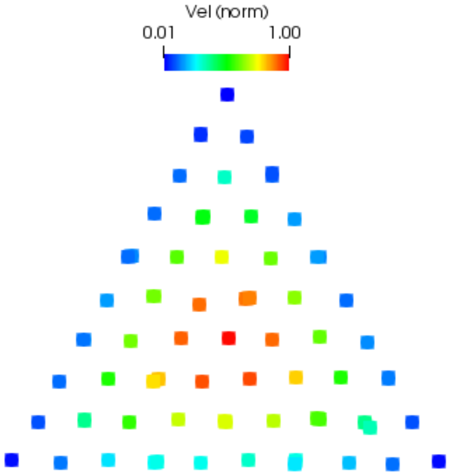

Figure 6: Cross-sectional slice of the fluid 3-D domain, normalised velocity of the shifted particle distribution for an equilateral triangular channel with Δx = 0.1m

As before, the initial particle distribution was random with $0.8\Delta x$ disturbance in all directions. Figure 6 shows the cross-sectional slice of the fluid 3-D domain at $t = 20.0$ sec with the thresholds of $\delta x_{max} = 10^{-4}$ and $\nabla C_{max} = 10^{-2}$. The fluid 3-D domain with the normalised velocity of the shifted particle distribution is shown in Figure 7.

Similar to the flow in a rectangular channel, particles have recovered a regular near-Cartesian particle distribution. Furthermore, the L_2 error norm in the horizontal velocity is shown in Figure 10 with a rate of convergence of 1.8.

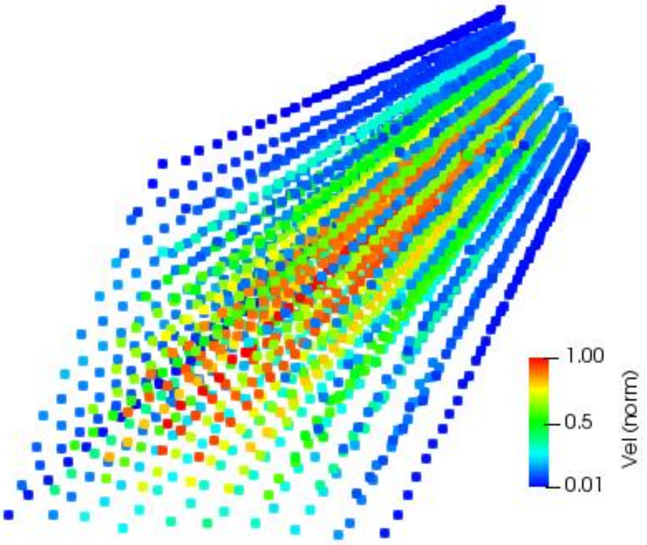

Figure 7: The fluid 3-D domain with the normalised velocity of the shifted particle distribution for an equilateral triangular channel with Δx = 0.1 m

3.2.3 Hagen-Poiseuille flow

The classical Hagen-Poiseuille flow with a radius $r = 0.5$ m and length of 5.0 m is simulated with a Reynolds number of $Re = 30$ and dynamic viscosity of $\mu = 10^{-2}$ Pa s. Three different particle resolutions have been used with $\Delta x = 0.1$, 0.05 and 0.025 m with the G4 kernel. Figure 8 shows the particle distribution after the end of the simulation at $t = 20.0$ sec with the thresholds of $\delta x_{max} = 10^{-6}$ and $\nabla C_{max} = 10^{-4}$, whereas Figure 9 shows the fluid 3-D domain with the normalised velocity for the shifted particle distribution. Although the distribution is not fully regular as in a Cartesian grid, the fluid particles follow the radial distribution of the wall boundary particles and the order of convergence remains close to 1.7 as shown in Figure 11.

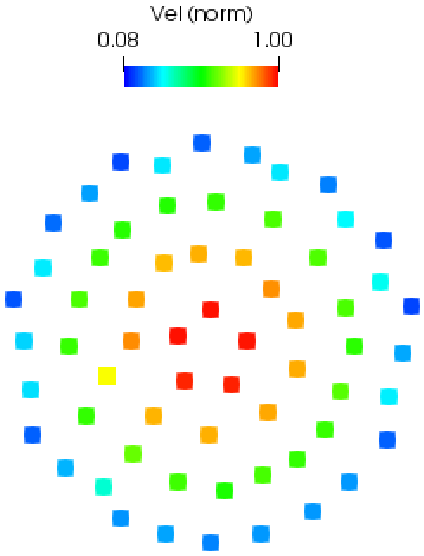

Figure 8: Cross-sectional slice of the fluid 3-D domain, normalised velocity of the shifted particle distribution for a circular channel with Δx = 0.1 m

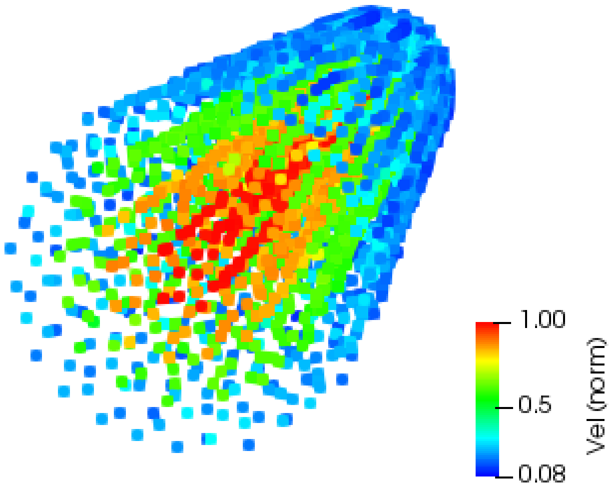

Figure 9: The fluid 3-D domain with the normalised velocity of the shifted particle distribution for the Hagen-Poiseuille flow with Δx = 0.1 m

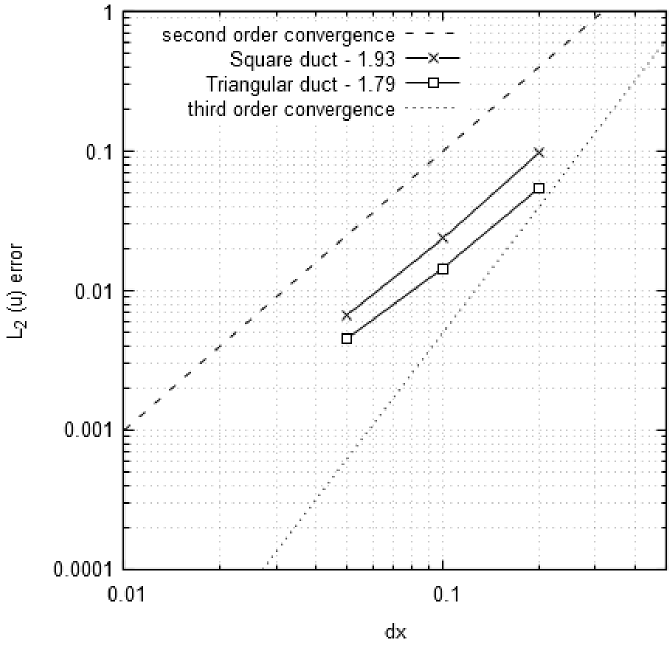

Figure 10: L_2 error norm in the horizontal velocity for the rectangular and the triangular channel using the Quinitic kernel with the wall boundary conditions of Adami *et al.* [19]

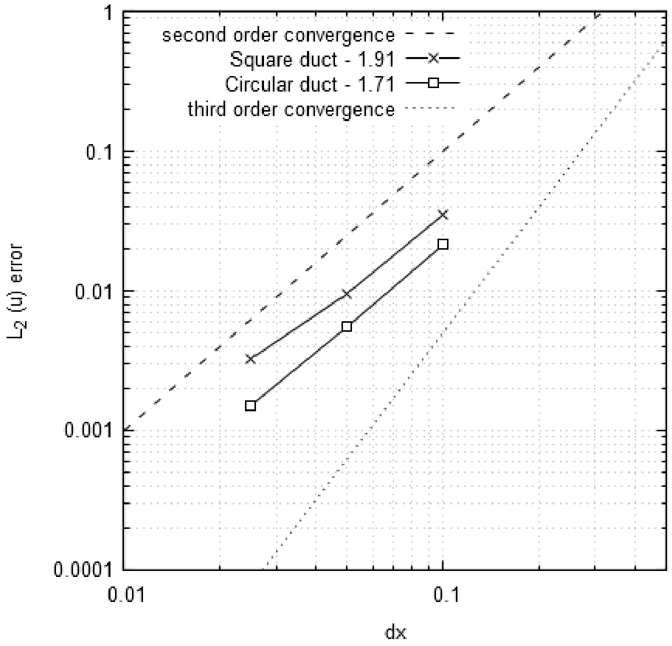

Figure 11: L_2 error norm in the horizontal velocity for the rectangular and the circular channel using the G4 kernel with the wall boundary conditions of Adami *et al.* [19]

In the above 3-D test cases, the effectiveness of the iterative shifting mechanism to recover near isotropic particle distribution with satisfactory convergence has been demonstrated. The numerical experiments show that the initial random distribution tends to follow the wall boundary particle discretisation as with the 3-D Hagen-Poiseuille flow. These results are in agreement with the findings of Vacondio and Rogers [18]. The use of the Quadratic kernel with a second convergence criteria avoided the error associated with particle clamping in the shifted domain and ensures that the error in the kernel interpolation remains low after the shifting procedure.

4 Higher-order Boundary Conditions

4.1 Introduction

A variety of wall boundary models are available for SPH ranging from dummy particle techniques [19], mirror wall boundaries [8], fictitious stencil boundary models [25], repulsive force boundaries [26] to semi-analytical wall boundary models [27]. However, these methods all suffer from currently being limited to second-order spatial accuracy. The afore-mentioned models can be split into two major categories (when excluding repulsive force methods):

1. Extensive models: These extend the computational domain into the boundary domain such that the smoothing kernel support for fluid particles near the boundary is filled with boundary particles. The properties of these boundary particles are assigned according to fluid properties near the wall to affect Dirichlet and/or Neumann boundary conditions.
2. Renormalisation techniques: These account for kernel truncation near boundaries by discretising the boundary into a number of surface particles and incorporating a normalisation factor that is designed to complete the support of kernel interpolations without using boundary particles. Dirichlet and Neumann BCs can also be enforced via this group of boundary models.

Takeda *et al*. [28] outlined a technique for enforcing Dirichlet velocity BCs for walls to second-order accuracy. This technique was intended for the extensive group of SPH wall boundary models. Other extensive models [19] and re-normalisation techniques [27] have also been shown to be near second-order accurate in space. However, to date no model has been shown to be higher-order accurate and no higher-order accurate SPH simulations have been demonstrated.

This is understandable given that the Lagrangian SPH formulation is at best second-order accurate [11] and its accuracy suffers greatly when the particle distribution becomes disordered, an unavoidable fact even when corrective particle shifting techniques (see [29] and [30]) are utilised.

The advent of Eulerian SPH ([6], [31]) and the fact that the method was shown to be capable of higher-order accuracy prompted the development of high-order accurate boundary conditions [31] which is the focus of this work. In a Eulerian frame, particle positions remain fixed in space and the problem of maintaining a uniform particle distribution is eliminated. Thus as long as the computational domain is discretised into a uniformly distributed set of particles with appropriate geometrically scaled volumes high-order convergence can be achieved.

4.2 Second- and high-order accuracy in SPH

A number of researchers (e.g. [32], [33] and [6]) have shown that the accuracy of the smoothing kernel interpolations can be improved to higher-order accuracy by re-normalising the smoothing kernel function such that even order error terms in the SPH approximation are removed. The SPH interpolation error can be written as

$$F_i = F_i \int W dV + h \int F_i^{'} q W dV + \frac{h^2}{2!} \int F_i^{''} q^2 W dV \\ + \frac{h^3}{3!} \int F_i^{'''} q^3 W dV + O(h^4) \qquad (10)$$

The odd-order (in *h*) error terms in Equation 10 cancel out due to the symmetry of smoothing kernel functions. However, the even order terms must be removed to attain higher-order accuracy. Creation of fourth-order accurate kernel functions may be accomplished as shown by Lind and Stansby [6] via deriving a new kernel function. This kernel function may be written as $W^{O4}(q)=(A-Bq^2)W(q)$, where W^{O4} is a fourth-order accurate version of the original kernel function, $q=\Delta r/h$ where Δr is the particle spacing and W is the original kernel function. Constants A and B can be evaluated by solving the following equalities

$$\begin{gathered}\int (A+Bq^2)q^2 W dV = 0 \\ \int (A+Bq^2) W dV = 1\end{gathered} \tag{11}$$

This leads to elimination of the $O(h^2)$ term in Equation 10 thereby making the approximation fourth-order accurate. This procedure was used in this work to create a new compactly supported fourth-order accurate kernel function based on the fifth-order polynomial Wendland function [34]. It must be noted that in order to achieve higher-order accuracy with a higher-order accurate kernel function, kernel correction techniques such as [35] may not be used as they render it asymmetric which brings the odd order error terms back into the equation since they do not cancel out.

4.3 High-order accurate MFD boundary conditions

In this section, the high-order accurate Mixed Finite Difference (MFD) extrapolation technique is presented.

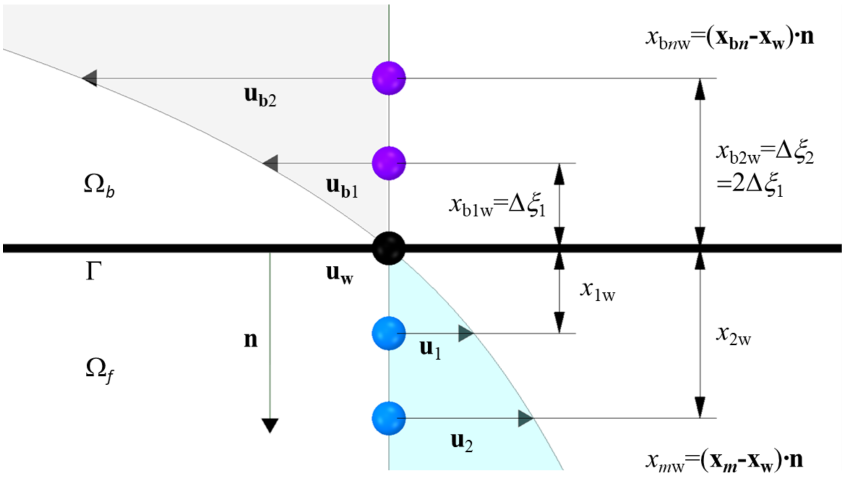

Figure 12: MFD wall boundary condition schematic for a flat surface

For the computational stencil shown in Figure 12, Ω_b represents the boundary domain, Ω_f represents the fluid domain and Γ represents the boundary surface (which can be a wall or an open boundary). The velocities of fluid particles 1 and 2, $\mathbf{u}_1$ and $\mathbf{u}_2$, are known from solving the governing equations and so is the velocity of the surface particle w ($\mathbf{u}_w$) which is prescribed for the case of wall surfaces with known velocities. For Eulerian SPH, it can also be ensured that particles in the stencil are arranged on a straight line and distributed uniformly along the stencil. Therefore, a combination of forward and backward finite difference interpolations can be utilised to affect the desired boundary conditions as detailed in [31]. Using this MFD technique, the following third-order accurate extrapolation can be performed to evaluate the boundary particle velocities

$$\begin{gathered}\mathbf{u}_{bn} = \mathbf{u}_w + x_{bnw}\frac{\mathbf{u}_1-\mathbf{u}_w}{x_{1w}} + \\ \left(\frac{{x_{bnw}}^2 - x_{bnw}x_{1w}}{2}\right)\left(\frac{\mathbf{u}_2-2\mathbf{u}_1+\mathbf{u}_w}{{x_{1w}}^2}\right) + O(\Delta\xi^3)\end{gathered} \tag{12}$$

where $\Delta\xi$ is the normal distance from the boundary particle to the wall surface. This extrapolation obeys the Dirichlet BC on the wall ($\mathbf{u}=\mathbf{u}_{\mathrm{w}}$) and also enforces a third-order accurate Dirichlet BC for wall boundary particles. For open boundaries, the wall particle in Figure 12 represents the fluid particle lying on the opening surface and the same procedure can be used to extrapolate the fluid velocities into the open boundary domain thereby setting the velocity values for opening boundary particles. For the third-order MFD wall and open BC models only two fluid particles are required. However, the fourth-order accurate variant of the MFD model requires three particles. The fourth-order accurate formulation reads

$$\mathbf{u}_{\mathrm{b}n} = \mathbf{u}_{\mathrm{w}} + \frac{x_{\mathrm{b}n\mathrm{w}}}{x_{1\mathrm{w}}} \left(\begin{array}{l} \dfrac{\mathbf{u}_3}{3} - \dfrac{3\mathbf{u}_2}{2} + 3\mathbf{u}_1 - \dfrac{11\mathbf{u}_{\mathrm{w}}}{6} + \\ \dfrac{x_{\mathrm{b}n\mathrm{w}}}{x_{1\mathrm{w}}} \left(\begin{array}{l} -\dfrac{\mathbf{u}_3}{2} + 2\mathbf{u}_2 - \dfrac{5\mathbf{u}_1}{2} + \mathbf{u}_{\mathrm{w}} + \\ \dfrac{x_{\mathrm{b}n\mathrm{w}}}{6x_{1\mathrm{w}}} \left(\mathbf{u}_3 - 3\mathbf{u}_2 + 3\mathbf{u}_1 - \mathbf{u}_{\mathrm{w}} \right) \end{array} \right) \end{array} \right) \tag{13}$$

$$+O(\Delta\xi^4),$$

where $\mathbf{u}_3$ is the velocity of the third fluid particle from the wall.

Higher-order accurate variants can be readily built using the methodology in [31] however for each increment in order of accuracy information from an additional fluid particle is required.

Implementing this technique requires that the boundary surface is first discretised into a uniformly distributed set of wall particles *w*, their uniformity is necessary to ensure that the accuracy of higher-order kernel interpolations is maintained. Then, the surface particles are used to generate the required number of fluid particles (two for the third-order variant or three for the fourth-order variant). These fluid particles must lie on the normal vector emanating from the wall particle $\mathbf{n}_{\mathrm{w}}$ and also be uniformly spaced. According to the desired value for $h/\Delta r$ a number of boundary particles must be generated to complete the support of the kernel function and also lie along $\mathbf{n}_{\mathrm{w}}$.

This procedure is repeated for all surface particles (lying on the wall surface or open boundary). Fluid particles not involved in the stencil may be distributed in a different manner; however, the volumes and positions of fluid particles not required for the stencil must still be uniform enough to achieve the required level of accuracy. Figure 13 illustrates the MFD extrapolation stencil as discretised on curved surfaces.

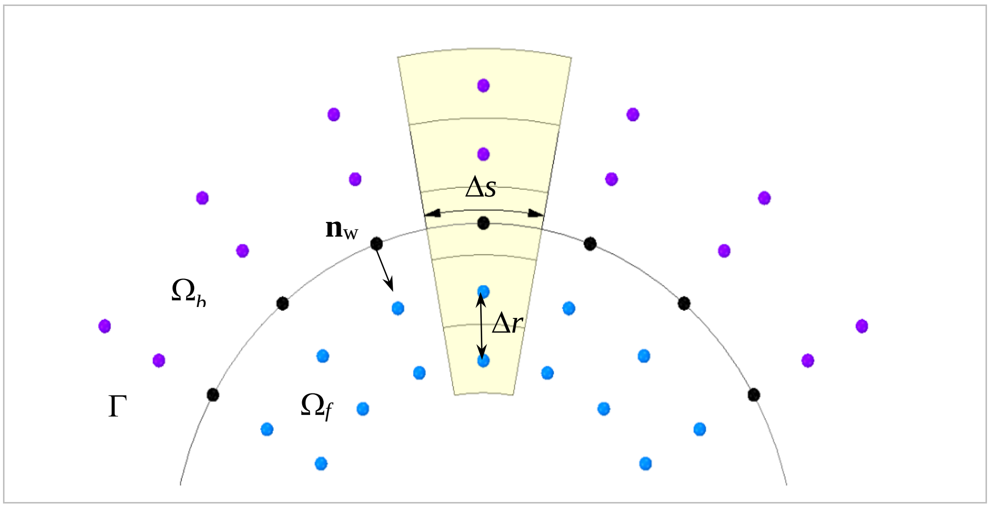

Figure 13: MFD wall boundary stencil near curved surfaces. The yellow curved volumes represent particle volumes in one stencil

For curved surfaces, the stencil requirements mean that particles in a given MFD stencil lying on a curved surface will inevitably have different volumes. While it is known that a uniform particle distribution is required to attain high-order accurate SPH interpolations [6], the results in this report show that higher-order accuracy is achievable even for non-uniform particle sizes provided the distribution is not purely random and that particle volumes accurately represent their geometric arrangement.

For the time being, the MFD boundary model has only been applied to flat or curved surfaces for which a uniform set of stencils can be generated, i.e. not surfaces involving sharp corners.

4.4 Convergence analysis

In this section, the high-order accurate MFD boundary conditions are validated and convergence of the Eulerian ISPH technique with the new boundary extrapolations is investigated.

4.4.1 Accuracy of kernel interpolations

In order to validate the accuracy of the velocity extrapolation to the wall and open boundary particles, the case of 3-D flow through a cylindrical annulus was used. Figure 14 shows the computational domain used for this study highlighting the fluid, wall and open domains. For these tests, the analytical solution of spiral flow through a cylindrical annulus was used.

In the domain shown in Figure 14, an external body force drives the fluid axially through the annular channel in the *y*-direction while the rotation of the inner and outer cylinders creates a secondary spiral flow. This complex 3-D flow was chosen to evaluate the ability of the wall boundary conditions to capture a fully 3-D flow with spatially varying velocity components in each Cartesian direction to fourth-order accuracy.

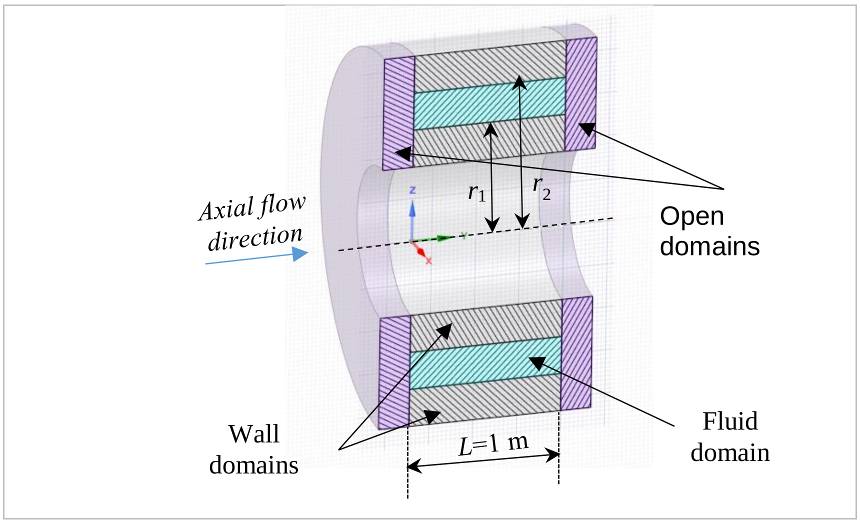

Figure 14: Cross-sectional schematic of computational domain

The radius of the inner cylinder is $r_1 = 1.5$ m with a constant angular velocity of $\Omega_1 = 0.1$ rad/s and the radius of the outer cylinder is $r_2 = 2$ m rotating in the same counter-clockwise direction with a constant angular velocity of $\Omega_2 = 0.025$ rad/s in the x - z plane. This results in a maximum tangential velocity for the inner cylinder of 0.15 m/s. Further, the external body force was applied to the *y*-direction with $a_y = 0.095868$ m/s^2 such that the maximum axial flow velocity was approximately 0.3 m/s.

The Reynolds numbers for the spiral and axial velocity were $Re_{Spiral} = 7.5$ and $Re_{axial} = 15$ respectively, based on the channel width $w = 0.5$ m as a characteristic length and the maximum tangential and axial velocities.

The domain was discretised using a radially distributed set of particles as shown in Figure 15, which includes the fluid and wall boundary particles. First the surface of the inner cylinder was discretised into a uniformly distributed set of particles with $\Delta\theta = 2\pi r_1/\Delta y$ where r_1 is the inner cylinder radius and Δy is the particle spacing along the annulus' axial direction. The surface particles were then extruded using a uniform radial spacing Δr along the wall normal vector to generate fluid and wall boundary particles lying along each surface particles' normal vector.

The particle spacing along the axial direction was set to $\Delta y = \Delta r$ meaning that although Δr and Δy is uniform there is quite a large variation of particle arc lengths Δs along the radial direction for each ring of particles. The particles used to discretise the inner surface have $\Delta s_1 = r_1 \Delta\theta$, while particles used to discretise the outer cylinder surface have an arc length of $\Delta s_2 = r_2 \Delta\theta$. For this test $r_1 = 1.5$ m while $r_2 = 2$ m meaning that $\Delta V_1/\Delta V_2 = 0.75$ where ΔV_1 and ΔV_2 are the volumes of particles lying on r_1 and r_2 respectively.

For particles used to discretise the wall domain the disparity in volume is even greater; the ratio between the minimum and maximum particle volumes used in this study for the lowest resolution test with $\Delta r = w/4$ is $\Delta V_{min}/\Delta V_{max} = 1/3$ based on the smallest inner wall boundary particle and the largest outer wall boundary particle. Three different particle spacings (resolutions) were used for this study; $\Delta r = w/4$, $\Delta r = w/6$ and $\Delta r = w/8$.

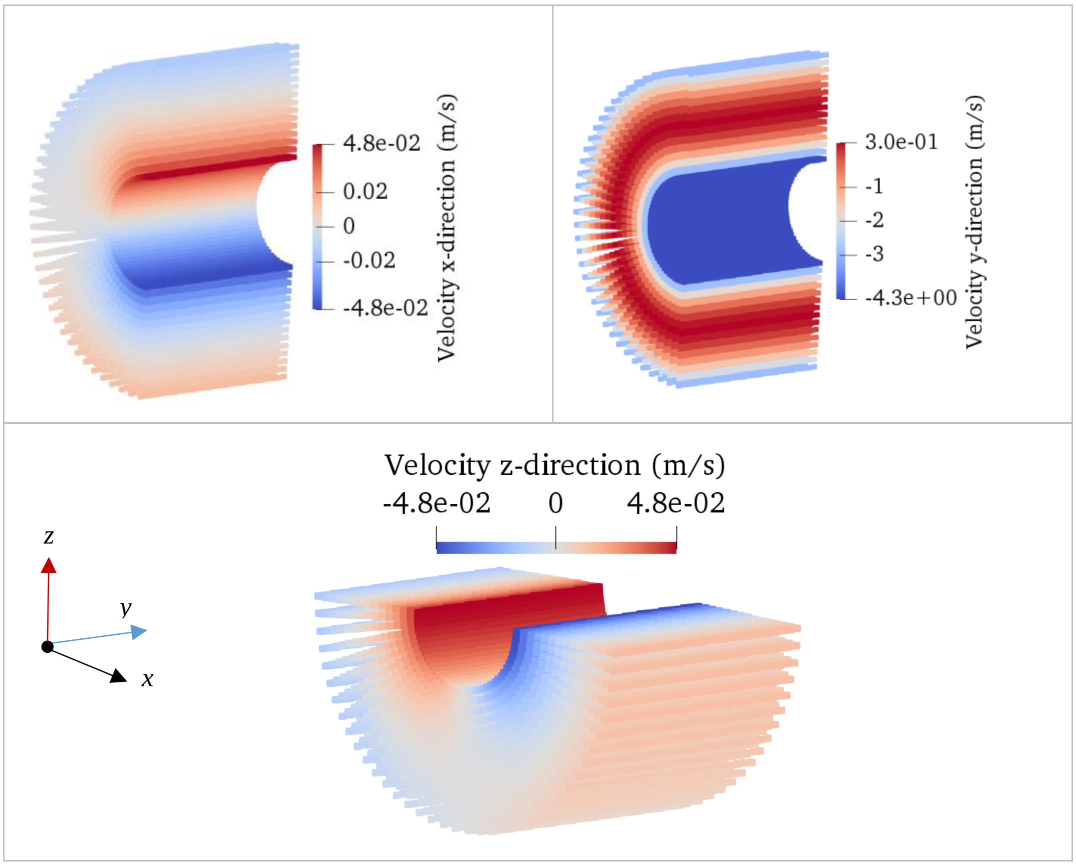

Figure 15: Cross-sectional views of the computational domain highlighting the Analytical velocity distribution for Δr=w/4

First, convergence of the smoothing kernel interpolation is assessed by assigning the analytical steady-state solution for velocity to each particle in the domain via

$$v_{axial}(r) = -\frac{a\rho}{4\mu}\left(\left(r_2^2 - r^2\right) - \left(r_2^2 - r_1^2\right)\frac{\ln(r_2/r)}{\ln(r_2/r_1)}\right)$$

$$u_{tan}(r) = \frac{1}{(r_2^2 - r_1^2)}\left(\begin{array}{c}\left(\Omega_2 r_2^2 - \Omega_1 r_1^2\right) r + \\ \dfrac{r_1^2 r_2^2(\Omega_1 - \Omega_2)}{r}\end{array}\right) \tag{14}$$

where v_{axial} is the axial flow velocity and u_{tan} is the tangential flow velocity w.r.t. the origin of the cylinders which is coincident for both inner and outer cylinders, $\rho = 1$ kg/m^3 and $\mu = 0.01$ Pa.s. Figure 15 shows the analytical velocity fields assigned to particles in the computational domain.

After assigning velocities to all particles in the fluid and boundary domains a kernel interpolation is performed to evaluate the velocity vector for each fluid particle as

$$\mathbf{u}_i = \sum_{j \in (\Omega_f \cup \Omega_b)} \mathbf{u}_j W_{ij} V_{ij} \tag{15}$$

where $\mathbf{u}_j$ for this test is the analytically prescribed velocity field. The error in the kernel interpolation is then quantified as

$$L_2^{norm} = \sqrt{\frac{1}{N_f}\sum_{i \in fluid}\left(\frac{U_{analytical} - U_i}{U_{analytical}}\right)^2} \tag{16}$$

where N_f is the number of fluid particles,

$$U_{i\ analytical} = \sqrt{(v_{i\ axial}^2 + u_{i\ \tan}^2)}$$

$$U_i = \sqrt{(u_i^2 + v_i^2 + w_i^2)} \tag{17}$$

and u_i, v_i and w_i are the interpolated velocities in the x, y and z Cartesian coordinates.

Figure 16 shows the L_2^{norm} error for the cases where the analytical velocity profile was used to evaluate the boundary particle velocities.

In these tests different values for the smoothing length were used ranging from $h = 2\Delta r$ to $h = 4\Delta r$. The observed order of convergence for these tests was roughly 0.5. Since the analytical solution is prescribed throughout the computational domain the only source of error is the smoothing kernel interpolation error which for the interpolated functions, Equation 14, has reached the limiting SPH discretisation error discussed by Quinlan *et. al.* [11].

As shown by Quinlan *et al*. [11] the SPH interpolation is $O(\Delta r/h)^{\alpha+2}$ where α is the kernel smoothness which is defined as the number of times the kernel is differentiable while remaining equal to zero at the edges of its support radius. The kernel used for these tests has a smoothness of $\alpha = 7$ hence the error is expected to be $O(\Delta r/h)^9$.

Figure 17 shows the error for interpolations performed using $h = 2\Delta r$, $3\Delta r$, $4\Delta r$ and $6\Delta r$ with a fixed $\Delta r = w/8$. The plot shows that the observed spatial accuracy of the interpolations is approximately $O(\Delta r/h)^{9.67}$ which is in agreement with the expected convergence rate of 9.

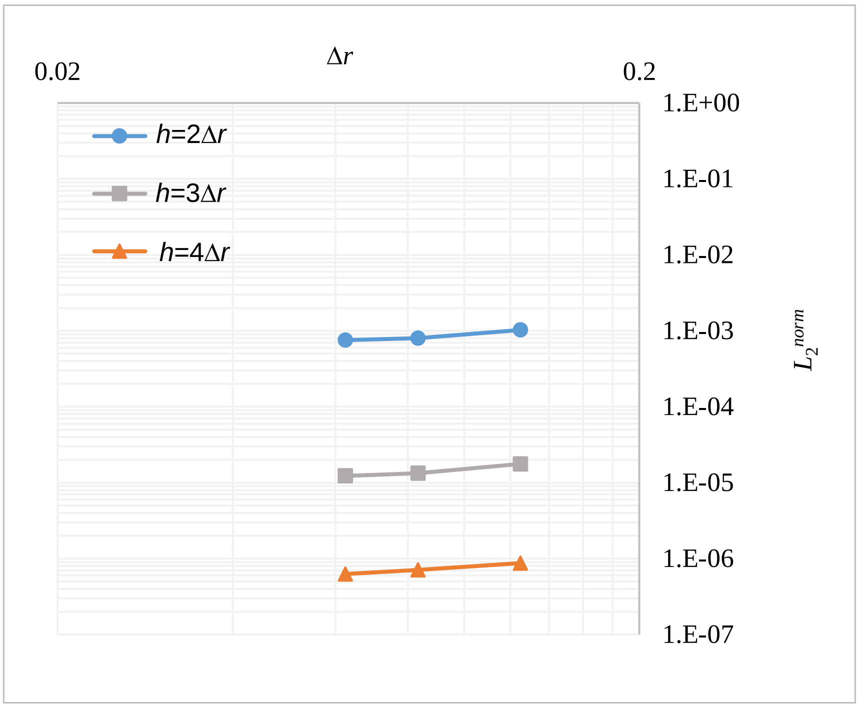

Figure 16: L_2^{norm} error vs radial particle spacing for the convergence study with analytical boundary velocities

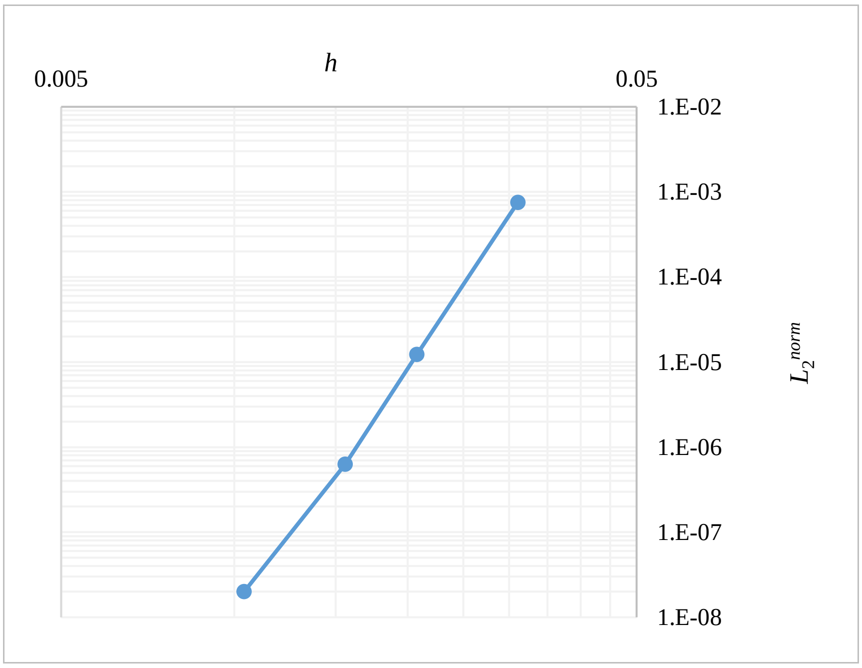

Figure 17: L_2^{norm} error vs *h* for the convergence study with analytical boundary velocities for a particle spacing of Δr = w/8

Extrapolating the velocity into the boundary domains will introduce additional error to the flow field in the boundary domains thereby increasing the global error, if this error is high enough the global error will be greater than the limiting SPH discretisation error.

Hence, another set of tests is performed to assess whether convergence can be achieved if the boundary velocities were extrapolated from the fluid particles using Equation 13 and then the fluid particle velocities were interpolated using Equation 15.

Figure 18 shows the convergence study results for the case with extrapolated boundary velocities. It may be noted that for the test with $h = 2\Delta r$ the solution has reached the limiting discretisation error limit. However, for the tests with $h = 3\Delta r$ and $h = 4\Delta r$ the error is converging following an approximately fourth-order trend, the exact convergence rates are 4.484 and 4.495, respectively.

These results show that SPH can be used to attain fourth-order accurate interpolations for wall bounded problems provided that fourth-order accurate boundary conditions are utilised and a fourth-order accurate kernel function. Based on these results, Section 4.4.2 demonstrates third-order convergence for full 3-D flow simulations with ISPH using the third-order variants of the MFD higher-order wall and open boundary conditions.

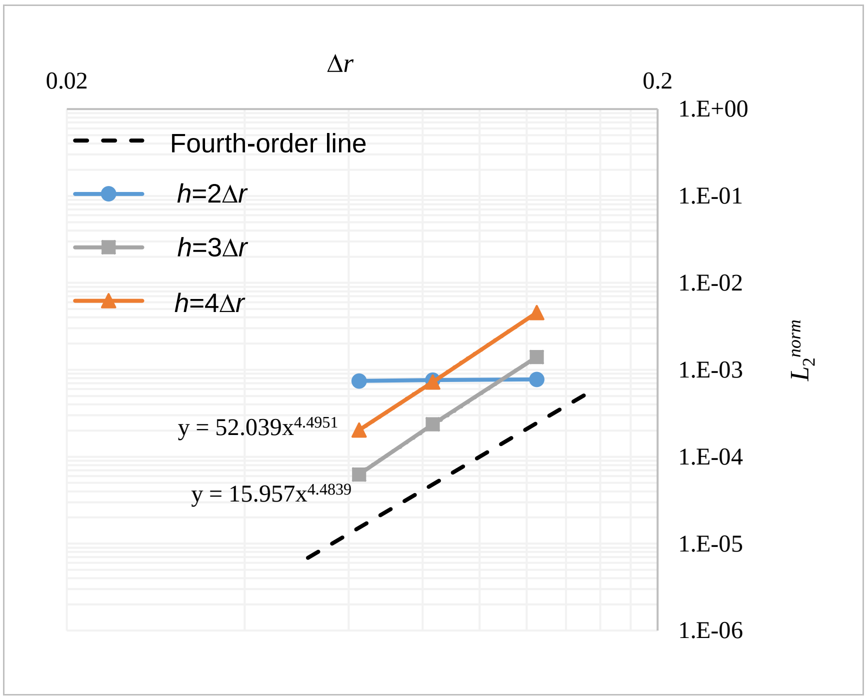

Figure 18: L_2^{norm} error vs radial particle spacing for the convergence study with extrapolated boundary velocities

4.4.2 Convergence study for a 3-D axial flow through an annulus

For these studies, the same annular computational domain shown in Figure 14 is used. However, for the full 3-D simulations only the axial component of the flow is simulated with the velocity of the inner and outer cylinder walls being set to u = (0, 0, 0) m/s.

Time integration of the ISPH algorithm is performed via the low-order projection method. Since the flow is axial and driven by an external body force, in-lieu of an axial pressure gradient, the pressures for the wall and open boundaries may be set to zero. The velocities however are extrapolated following the third-order MFD extrapolation in Equation 12.

The axial flow is started from the steady state analytical solution and the external body force is $a = 0.025$ m/s^2 while the fluid properties are $\rho = 1$ kg/m^3 and $\mu = 0.01$ Pa.s. The Reynolds number for this test was approximately $\mathrm{Re} = 3.9$ based on the maximum flow velocity of 0.0783 m/s and $w = 0.5$ m. The flow is simulated for $t = 20$ s for all cases.

At this point in time the L_2^{norm} error is virtually constant meaning that the numerical solution has reached a steady state. Three particle spacings (resolutions) were used for this study namely $\Delta r = w/3$, $\Delta r = w/5$ and $\Delta r = w/6$ with $h = 4\Delta r$. The time step was set using $\Delta t = C_u h / U_{\max}$ where

$C_u = 0.05$ and $U_{\max}$ is the maximum fluid velocity. A low value for the Courant constant C_u was used to lower the temporal integration error and allow the observation of spatial convergence.

Figure 19 shows the results of the error analysis performed using Equation 16 and the steady state solution for the three resolutions simulated with third-order extrapolated boundary velocities.

The convergence rate is approximately 3.01 for this test showing that the MFD high-order extrapolation is indeed capable of producing spatially third-order accurate ISPH simulations even when using lower-order accuracy time integration schemes provided that the time step size is sufficiently small.

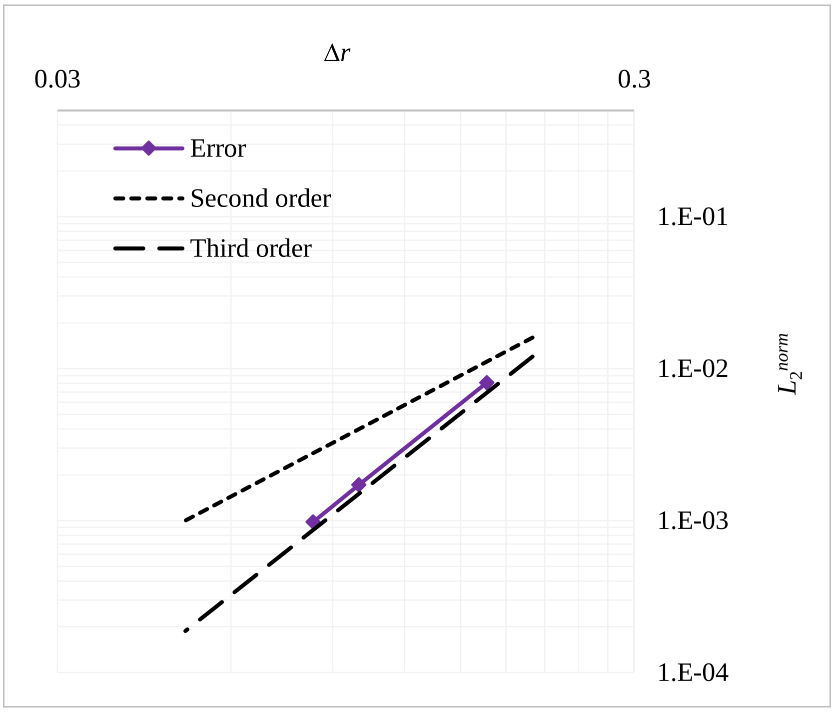

Figure 19: L_2^{norm} error vs radial particle spacing for the convergence study performed with three full 3-D simulations and third-order extrapolated boundary velocities

5 Arbitrary Lagrangian-Eulerian SPH

5.1 Introduction

The effect on stability and accuracy of anisotropic particle distributions and formation of coherent particle structures is well documented in smoothed particle hydrodynamics (SPH) [11, 36-39] and has a severe impact on the convergence characteristics of the scheme.

Several variants of the original SPH scheme [40] have been proposed to improve the accuracy of the solution by using kernel corrections which ensure zeroth- and first-order consistency for anisotropic particle distribution [36, 38]. However, the Lagrangian motion of the particles unavoidably generates coherent structures that follow the streamlines (if accurate enough). The recent developments of the diffusion-based particle shifting [7, 37, 41] acts to maintain a homogeneous particle distribution and improve the accuracy of the approximations.

Initially developed for incompressible SPH, the Fickian shifting approach has been very successful on single and multi-phase flows in weakly compressible SPH (WCSPH), examples include Vacondio *et al.* [42] in single phase flows, Mokos *et al.* [43] and Fourtakas and Rogers [44] in multi-phase flows and recently Sun *et al.* [45]. Sun *et al.* [46] added advection terms to the momentum and density conservation equations, without solving for the temporal volume evolution.

The conservation and consistency of the scheme can be maintained using an Arbitrary Lagrangian-Eulerian scheme in SPH formalism (ALE-SPH) as outlined by Vila [47]. Recently Oger *et al.* [15] embedded the particle shifting mechanism in the ALE-SPH formulation of Vila [47]. More recently Colagrossi *et al.* [48] demonstrated that a diffusive term has to be added to the mass and density equations to prevent too large volume particle variations. Notable is the work of Michel *et al.* [49] where a hybrid scheme ALE-SPH where the shifted and non-shifted ALE schemes is proposed.

Herein, a WCSPH scheme is proposed based on the consistent ALE formulation Vila [47] that preserves not only a near isotropic spacing and therefore, near to theoretical convergence rate provided by the kernel function, but also maintains stability in terms of volume. This is achieved by utilising the iterative shifting procedure of Vacondio and Rogers [50] to obtain the arbitrary velocity which results in a near isotropic particle distribution in space and thus, a constant volume field.

5.2 Numerical scheme

5.2.1 The Arbitrary Lagrangian-Eulerian framework

In order to establish the conservation laws of mass and momentum in an ALE formulation, the rate of change of a field function over a volume V_t bounded by a closed surface S_t is considered. It is assumed that the volume moves in time t with a velocity $\mathbf{u} = \mathbf{u}(\mathbf{x}, t)$ and the volume is constant, i.e. a material volume. It can be shown that the material or total time derivative of the integral of the field function $f = f(\mathbf{x}, t)$ over the volume in time is given by the Reynolds transport theorem [51],

$$\begin{aligned}\frac{d}{dt}\int_{V_t} f(\mathbf{x},t)dV &= \int_{V_c} \frac{\partial f(\mathbf{x},t)}{\partial t}dV \\ &+ \int_{S_c} f(\mathbf{x},t)\mathbf{u}\cdot\mathbf{n}dS\end{aligned} \qquad (18)$$

where $V_c \equiv V_t$ is an Eulerian volume fixed in space which coincides with the material volume and $S_c \equiv S_t$ is the equivalent of a fixed Eulerian surface at time t, **u** is the velocity vector and **n** the outward unit normal vector to the surface S_t. By using the Gauss theorem, the last term in the right-hand side of Equation 18 can be written as,

$$\int_{S_c} f(\mathbf{x},t)\mathbf{u}\cdot\mathbf{n}dS = \int_{V_c} \nabla\cdot\left(f\,\mathbf{u}\right)dV \tag{19}$$

which lead to the alternative Reynolds transport theorem,

$$\frac{d}{dt}\int_{V_t} f(\mathbf{x},t)dV = \int_{V_c}\left(\frac{\partial f(\mathbf{x},t)}{\partial t} + \nabla\cdot\left(f\,\mathbf{u}\right)\right)dV \tag{20}$$

The first term of the integral in the right-hand side of (3) is the local time derivative and the second term represents the flux of f in the Eulerian control volume. In a differential form, Equation 20 takes the familiar form of,

$$\frac{df(\mathbf{x},t)}{dt} = \frac{\partial f(\mathbf{x},t)}{\partial t} + \nabla\cdot\left(f\,\mathbf{u}\right) \tag{21}$$

In an ALE context, the characterising velocity is no longer the material velocity, but an arbitrary particle velocity denoted by $\hat{\mathbf{u}}$. Thus Equation 20 takes the following form,

$$\frac{d}{dt}\int_{V_t} f(\mathbf{x},t)dV = \int_{Vt}\left(\frac{\partial f(\mathbf{x},t)}{\partial t} + \nabla\cdot\left(f\,\hat{\mathbf{u}}\right)\right)dV \tag{22}$$

This implies that $S_t = \partial V_t$ and mass flux exchange is taking place in t with surrounding volumes. By substituting the local time derivative in the Euler equations of motion and collecting the terms, one can write,

$$\frac{d}{dt}\int_{V_t} \boldsymbol{\Phi}dV + \int_{V_t}\nabla\cdot\left(\mathbf{F} - \hat{\mathbf{u}}\otimes\boldsymbol{\Phi}\right)dV = 0 \tag{23}$$

where **Φ** and **F** is defined as the conservative (state) variables and the convective flux tensor and pressure respectively,

$$\boldsymbol{\Phi} = \begin{pmatrix}\rho \\ \rho\mathbf{u}\end{pmatrix}, \qquad \mathbf{F} = \begin{pmatrix}\rho\mathbf{u} \\ \rho\mathbf{u}\otimes\mathbf{u} + P\mathbf{I}\end{pmatrix} \tag{24}$$

where ρ is the density, P is the pressure and **I** the unit tensor.

Finally, the differential form of Euler equations in conservative ALE form reads,

$$\frac{d(V\boldsymbol{\Phi})}{dt} + V\nabla\cdot\left(\mathbf{F} - \hat{\mathbf{u}}\otimes\boldsymbol{\Phi}\right) = 0 \tag{25}$$

5.2.2 The ALE weakly compressible SPH formalism

Similar to the work of Vila [47], a conservative symmetric formulation is sought for the discretisation of the right hand side of Equation 25. Using the identity,

$$\nabla\left(\mathbf{F} - \hat{\mathbf{u}}\otimes\boldsymbol{\Phi}\right) = \nabla\left(\mathbf{F} - \hat{\mathbf{u}}\otimes\boldsymbol{\Phi}\right) + \left(\mathbf{F} - \hat{\mathbf{u}}\otimes\boldsymbol{\Phi}\right)\nabla 1 \tag{26}$$

the SPH discrete form of Equation 25 becomes [15],

$$\frac{d(V_i\boldsymbol{\Phi}_i)}{dt} = -V_i\sum_j\left(\mathbf{F}_i - \hat{\mathbf{u}}_i\otimes\boldsymbol{\Phi}_i + \mathbf{F}_j - \hat{\mathbf{u}}_j\otimes\boldsymbol{\Phi}_j\right)\cdot\nabla W_{ij}V_j \tag{27}$$

where subscript *i* and *j* denote the interpolating and neighbouring particles and subscripts *ij* the difference between the interpolating and neighbouring particles. From Equation 22, the evolution of particle volume can be written as,

$$\frac{dV_i}{dt} = V_i \sum_j \left(\hat{\mathbf{u}}_j - \hat{\mathbf{u}}_i \right) \cdot \nabla W_{ij} V_j \tag{28}$$

Note, the temporal evolution of a discrete particle in space now reads,

$$\frac{d\mathbf{x}}{dt} = \hat{\mathbf{u}}(\mathbf{x}, t) \tag{29}$$

Finally, the fully discretised Euler equations in a weakly compressible ALE SPH formalism read,

$$\begin{aligned} \frac{d\mathbf{x}_i}{dt} &= \hat{\mathbf{u}}_i \\ \frac{dV_i}{dt} &= V_i \sum_j \left(\hat{\mathbf{u}}_j - \hat{\mathbf{u}}_i \right) \cdot \nabla W_{ij} V_j \\ \frac{d(V_i \mathbf{\Phi}_i)}{dt} &= -V_i \sum_j \begin{pmatrix} \mathbf{F}_i - \hat{\mathbf{u}}_i \otimes \mathbf{\Phi}_i + \\ \qquad \mathbf{F}_j - \hat{\mathbf{u}}_j \otimes \mathbf{\Phi}_j \end{pmatrix} \cdot \nabla W_{ij} V_j \end{aligned} \tag{30}$$

To recover the Navier-Stokes equation the viscous forces in Equation 30 are discretised using the Morris operator [8] defined by,

$$V \mu \Delta \mathbf{u} = 2V_i \sum_j \mu \frac{\mathbf{r}_{ij}}{r_{ij}^2} \cdot \nabla W_{ij} \mathbf{u}_{ij} V_j \tag{31}$$

As in the Lagrangian weakly compressible SPH formalism, a sub-closure model is used to link pressure to density by the Morris equation as,

$$P = c_0^2 \left(\rho - \rho_0 \right) \tag{32}$$

allowing for a 1% variation in density by the following relationship $\rho = m / V$. The speed of sound c_o is defined as $c_0 \geq 10 U_{max}$ where U_{max} is the maximum fluid velocity of the domain.

The time integration scheme is an explicit predictor-corrector scheme [52] bounded by the CFL condition [53]. Note that, the CFL condition uses the physical velocity **u** and not the arbitrary velocity.

Finally, two kernels have been used in this work to demonstrate second- and fourth-order convergence rates, the Wendland kernel defined as,

$$W(r,h) = a_d \left(1 - \frac{r}{2h} \right)^4 \left(2\frac{r}{h} + 1 \right) \tag{33}$$

with $r = |\mathbf{x} - \mathbf{x}'|$ and a normalisation constant $a_d = 7/4h\pi^2$ and the compactly supported Gaussian G4 as,

$$W(q,h) = a_d \left(1 - \frac{r^2}{2h^2} \right) \exp(-r^2 / h^2) \tag{34}$$

where $q = |\mathbf{x} - \mathbf{x}'| / h$ and a normalisation constant $a_d = 2/\pi h^2$, respectively.

5.3 Arbitrary velocity based on an iterative shifting procedure

In order to reduce the spatial anisotropy of particles by forming coherent particle structures as the accuracy of the Lagrangian discretisation scheme is increasing, a number of methodologies have been developed [7, 37, 39, 54].

In general, these schemes update the position of particle *i* by,

$$\mathbf{x}_{s,i}^{n+1} = \mathbf{x}_i^{n+1} + \delta\mathbf{x}_i \qquad (35)$$

where the term **δx** is a shifting distance and the subscript *s* the shifted final particle position. In the diffusion-based scheme of Lind *et al.* [37] the shifting distance is a function of the gradient of the concentration gradient such as,

$$\delta\mathbf{x}_i = -Ah^2\nabla C_i \qquad (36)$$

where A is problem dependent constant and taken equal to 0.2 and ∇C_i is simply the derivative of the zeroth moment defined as,

$$\frac{dC_i}{dt} = \sum_j V_j \nabla W_{ij} \qquad (37)$$

To overcome the conservation and consistency issues associated with the Fickian shifting, Oger *et al.* [15] and lately Colagrossi *et al.* [48] embedded a shifting procedure within an ALE scheme. However, Equation 35 was solved explicitly, with no control adopted on the particle distribution generated by the shifting correction.

Vacondio and Rogers [50] and more recently Fourtakas *et al.* [55], recognised that the correction $\delta\mathbf{x}_i$ calculated using Equation 36, does not guarantee that the obtained particle distribution guarantee sufficient accuracy for SPH spatial interpolation at the next time step. They proposed an iterative shifting procedure to minimise the error of the SPH spatial interpolation. When particle position needed to be corrected the diffusion shifting was applied iteratively until, a minimum predefined limit in ∇C_i and the pre-defined error associated with the SPH approximation of a polynomial function has been reached.

This can be demonstrated by considering the SPH kernel derivative approximation of a field function *f* defined in **x** of a particle *i* in a discrete form, as,

$$\begin{aligned}\frac{\partial f(\mathbf{x}_i)}{\partial \mathbf{x}} = f(\mathbf{x}_i)\sum_j \frac{\partial W_{ij}}{\partial \mathbf{x}} V_j &+ \\ \frac{\partial f(\mathbf{x}_i)}{\partial \mathbf{x}} \sum_j (\mathbf{x}_j - \mathbf{x}_i) \frac{\partial W_{ij}}{\partial \mathbf{x}} V &+ \ldots + O(h)^n\end{aligned} \qquad (38)$$

In Equation 38, as $\nabla C_i \rightarrow 0$ the first term on the right-hand side vanishes which is the major source of error in the SPH approximation. The second term shows the error associated with the ability of the kernel derivative to approximate polynomials up to *n*th order as discussed by Fourtakas *et al.* [55]. For details of the iterative shifting procedure the reader is directed to Vacondio and Rogers [50] and Fourtakas *et al.* [55].

Although the iterative shifting procedure reduces the spatial discretisation error, it deems the scheme non-conservative as particles are disturbed from their Lagrangian trajectories. To overcome the issue of conservation and consistency the ALE scheme is adopted in this report. Similar to Colagrossi *et al.* [48] the scheme does not employ Riemann solvers with an implicit diffusion of fluxes.

Herein, the arbitrary velocity is defined as,

$$\hat{\mathbf{u}}(\mathbf{x},t) = \frac{\delta \mathbf{x}_i}{\Delta t} \tag{39}$$

which is simply the shifting velocity of the iterative shifting procedure. The term $\delta\boldsymbol{x}_i$ is measured as the difference of the final shifted position from the original position of particle *i*. Assuming an initial domain discretised in equal volumes, the iterative shifting arbitrary velocity guarantees that the volume flux between particles is minimised. As with Vacondio and Rogers [50] the iterative shifting arbitrary velocity can be calculated only when the threshold error is exceeded in ∇C_i or when the discretisation error of the gradient of a polynomial reaches an upper limit as with Fourtakas *et al.* [55].

5.4 Numerical results

5.4.1 Taylor-Green vortices

The Taylor-Green vortices test case consists of an unbounded periodic 2-D domain. The domain is initialised by a smoothed distribution of counter rotating vortices with temporal and spatial decay.

The solution of Equation 23 is for a strictly incompressible fluid. The test case has been used extensively in the past to test the effectiveness of shifting methodologies and algorithms [7, 15, 37, 42, 56]. The square domain with dimensions of 1 m × 1 m is initialised with the following velocity and pressure field,

$$\begin{aligned} u &= -e^{f}\cos(2\pi x)\sin(2\pi y) \\ v &= e^{f}\sin(2\pi x)\cos(2\pi y) \\ p &= -\frac{e^{2f}}{2}\left(\cos(4\pi x)+\cos(4\pi y)\right) \end{aligned} \tag{40}$$

where $f = -8\pi^2 t/\mathrm{Re}$. The Reynolds number takes the usual form of $\mathrm{Re} = \rho LU/\mu$, where U = 2 m/s is the maximum initial velocity at t = 0 sec, L is the characteristic length and the dynamic viscosity is μ = 0.01 Pa.s. The initial density was set to ρ_0 = 1.0 kg/m^3 and particle spacing of dx = 0.025 m using the Wendland kernel of Equation 33 with a smoothing length of h = 2.0dx. Herein, the initial particle distribution is Cartesian. At t = 2.0 sec, Figure 20(a), shows the relative error in the velocity magnitude defined as,

$$\bar{u} = \frac{|u_{SPH} - U|}{U} \tag{41}$$

for the ALE formulation with purely Lagrangian transport velocity, by setting the arbitrary velocity equal to the physical velocity $\mathbf{u} = \hat{\mathbf{u}}$ thus, recovering a constant particle mass. In Figure 20(b), the arbitrary velocity in the ALE scheme is computed by using one iteration of the Fickian particle shifting algorithm in a similar manner to Colagrossi *et al.* [48]. Finally, Figure 20(c) shows the relative error in the velocity magnitude for the proposed ALE with iterative shifting (ALE-IS). Clearly, the error in the latter is significantly smaller by more than an order of magnitude than the ALE scheme with one iteration or the ALE scheme using a Lagrangian transport velocity.

Similar results are shown on the right hand side of Figure 20 for the relative error in the pressure field using the equivalent form of Equation 41. It should be noted that the pressure field of the ALE scheme with Lagrangian transport velocity and ALE with one iteration has become unstable.

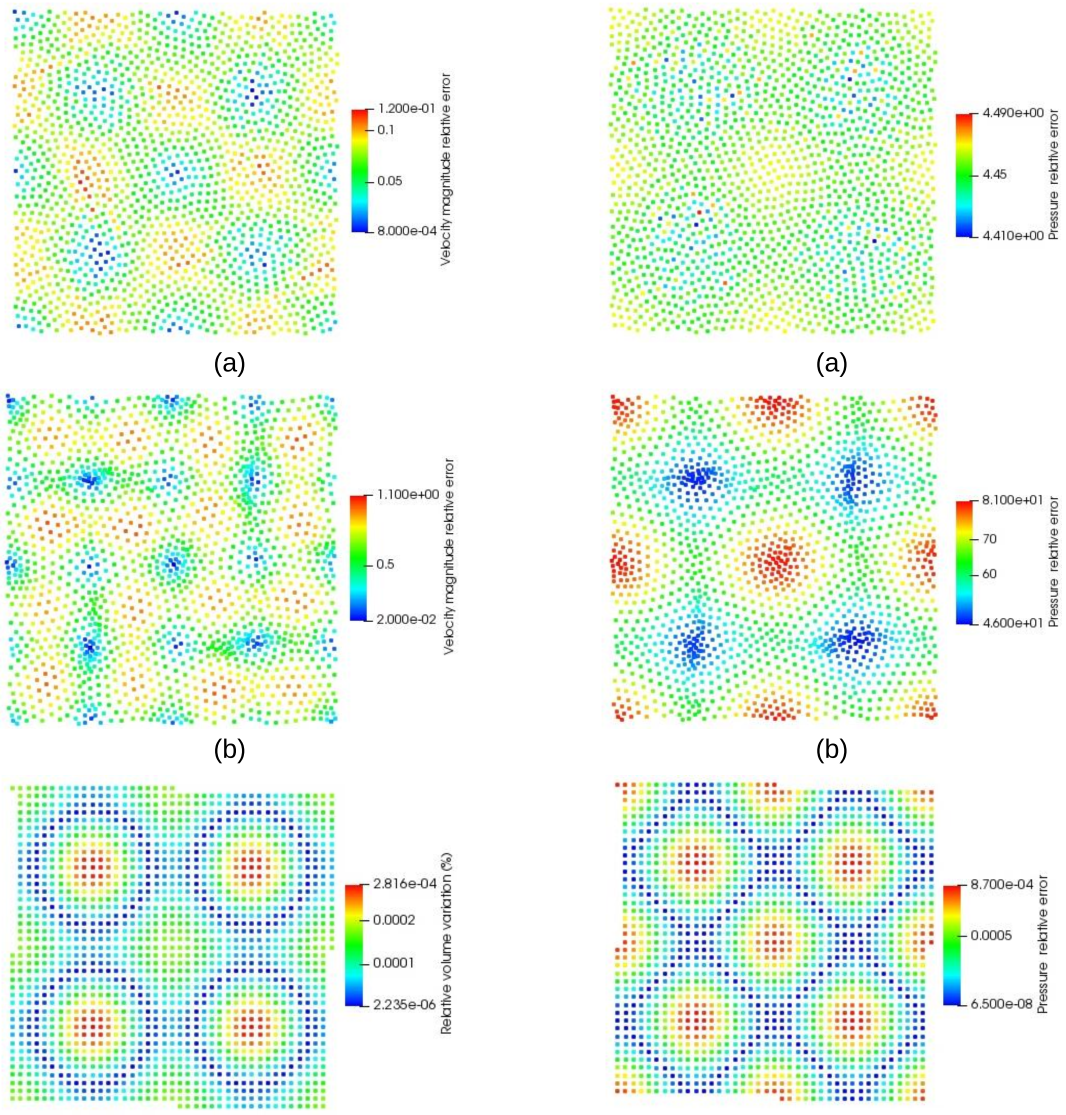

(a) (a)

(b) (b)

(c) (c)

Figure 20: Taylor-Green vortices relative error in the velocity magnitude (left) and pressure (right) at t = 2.0 sec with Re = 100 and particle resolution of dx = 0.025 m for (a) the ALE scheme with a Lagrangian transport velocity, (b) the ALE scheme with one shifting iteration and (c) the proposed ALE-IS scheme

An interesting result is the volume variations obtained using the equivalent of Equation 41 presented as a volume variation percentage and the particle distribution at t = 2.0 sec for the two ALE variants. Figure 21(a) and Figure 21(b) shows the percentage of volume variations for the ALE scheme with one shifting iteration and the proposed ALE-IS scheme.

In Figure 21(a), one can observe large volume fluxes in regions of high strain rate from the surrounding particles in the ALE scheme with one shifting iteration, also evident by the particle distribution. Note: no diffusive terms have been used in the governing equations for any of the ALE variants. The findings are similar to the work of Colagrossi *et al.* [48] that observed large volume fluxes which deemed the SPH operators inaccurate in the absence of numerical diffusion terms. In contrast, the ALE-IS scheme in Figure 21(b) shows an almost constant volume field due to the iterative shifting algorithm.

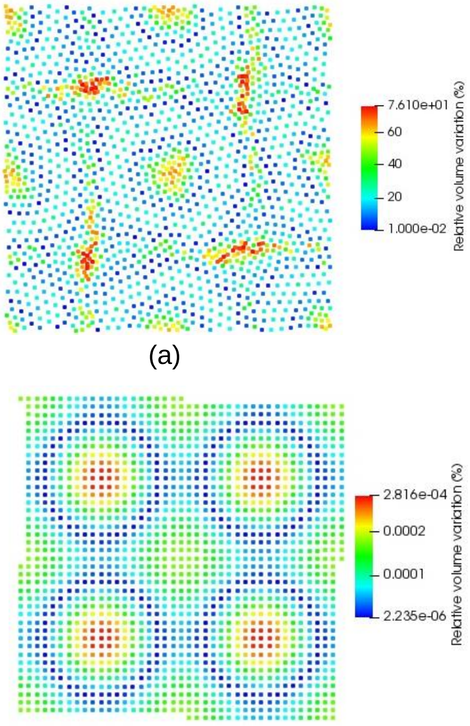

(a)

(b)

Figure 21: Taylor-Green vortices percentage of volume variations and spatial particle distribution for (a) the ALE scheme with one shifting iteration and (b) the proposed ALE-IS scheme, at *t* = 2.0 sec with *Re* = 100

A convergence study has been conducted to assess the accuracy and convergence characteristics of the proposed ALE-IS scheme. Figure 22 shows the spatial convergence rates for the Taylor-Green vortices using the Wendland kernel of Equation 33. A convergence rate of 1.9 is achieved for the velocity and pressure near the theoretical convergence rate of the kernel.

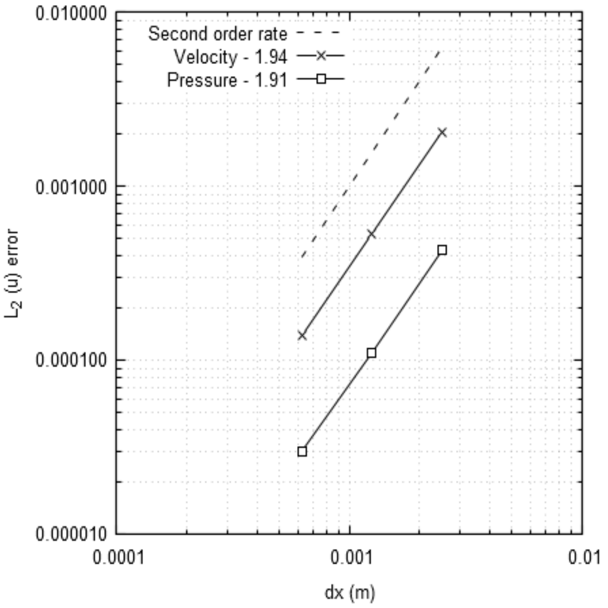

Figure 22: Spatial convergence rates for the Taylor-Green vortices using the Wendland kernel at t = 2.0 sec

5.4.2 Inviscid wall bounded vortex

As described by Vacondio and Rogers [50], a bounded weakly compressible vortex, is simulated in a circular domain. The initial density of the particle is $\rho_0 = 1.0$ kg/m^3 with an asymptotic density of $\rho_M = 1.01$ kg/m^3. The desired weakly compressibility of the domain is achieved by setting the appropriate artificial speed of sound, in this case $c_0 = 1.0$ m/s using the Morris equation of state of Equation 32. The domain radius is 0.7 m with an initial particle spacing of $dx = 0.01$ m using the Wendland kernel of Equation 33 with a smoothing length of $h = 2.0dx$.

In the absence of a high order boundary condition, the appropriate number rows of dummy particles are used to represent the solid wall where the analytical velocity is imposed as,

$$u_\theta(r) = \frac{2r}{r_0} c_0 \sqrt{\frac{\rho_\mathrm{M} - \rho_0}{\rho_r} e^{-\frac{2r}{r_0}}} \tag{42}$$

where u_θ is the velocity in cylindrical coordinates $r_0 = 0.1$ m with the appropriate density and pressure [50].

In the Taylor-Green test case, the initial particle distribution was over a Cartesian grid. To demonstrate the effectiveness of the proposed ALE-IS scheme, an initial random particle distribution is used for the inviscid vortex as shown in Figure 23(a) with the final distribution at $t = 5.0$ sec shown in Figure 23(b). Although, the final distribution is not Cartesian, the ALE-IS error and convergence characteristics follow the ideal theoretical convergence rates as will be shown shortly.

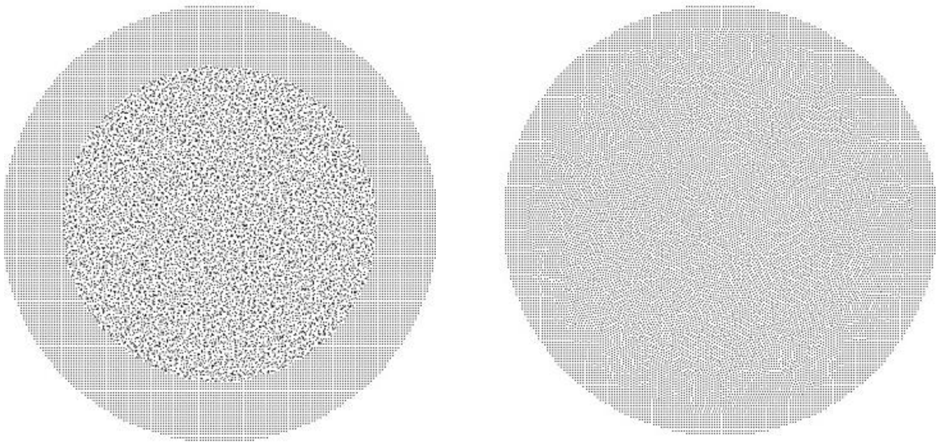

(a) (b)

Figure 23: (a) Initial particle distribution and final particle distribution after $t = 5.0$ seconds for the inviscid vortex test case

Figure 24(a), (b) and (c) shows the relative error in velocity magnitude, pressure and volume respectively for the ALE scheme with one shifting iteration at time $t = 2.2$ sec before going unstable. Notably, the error in velocity and pressure is unacceptable, as the volume variations seen in Figure 24(c) resulted in cluster particles. This result is in-line with the Taylor-Green vortices (Section 5.4.1) where similar behaviour was observed originating from the clustered particles, which deem the simulation inaccurate.

In contrast, Figure 24(d), (e) and (f) shows the relative error in velocity magnitude, pressure and volume respectively for the proposed ALE-IS scheme at $t = 5.0$ sec. Clearly, the improvement over the ALE scheme with one shifting iteration is substantial. Note: the initial particle distribution was random which would incur large errors in the SPH gradient. Nevertheless, by using the ALE-IS scheme, at the end of the simulation, the particle distribution is near isotropic with less than 0.01 % volume variation.

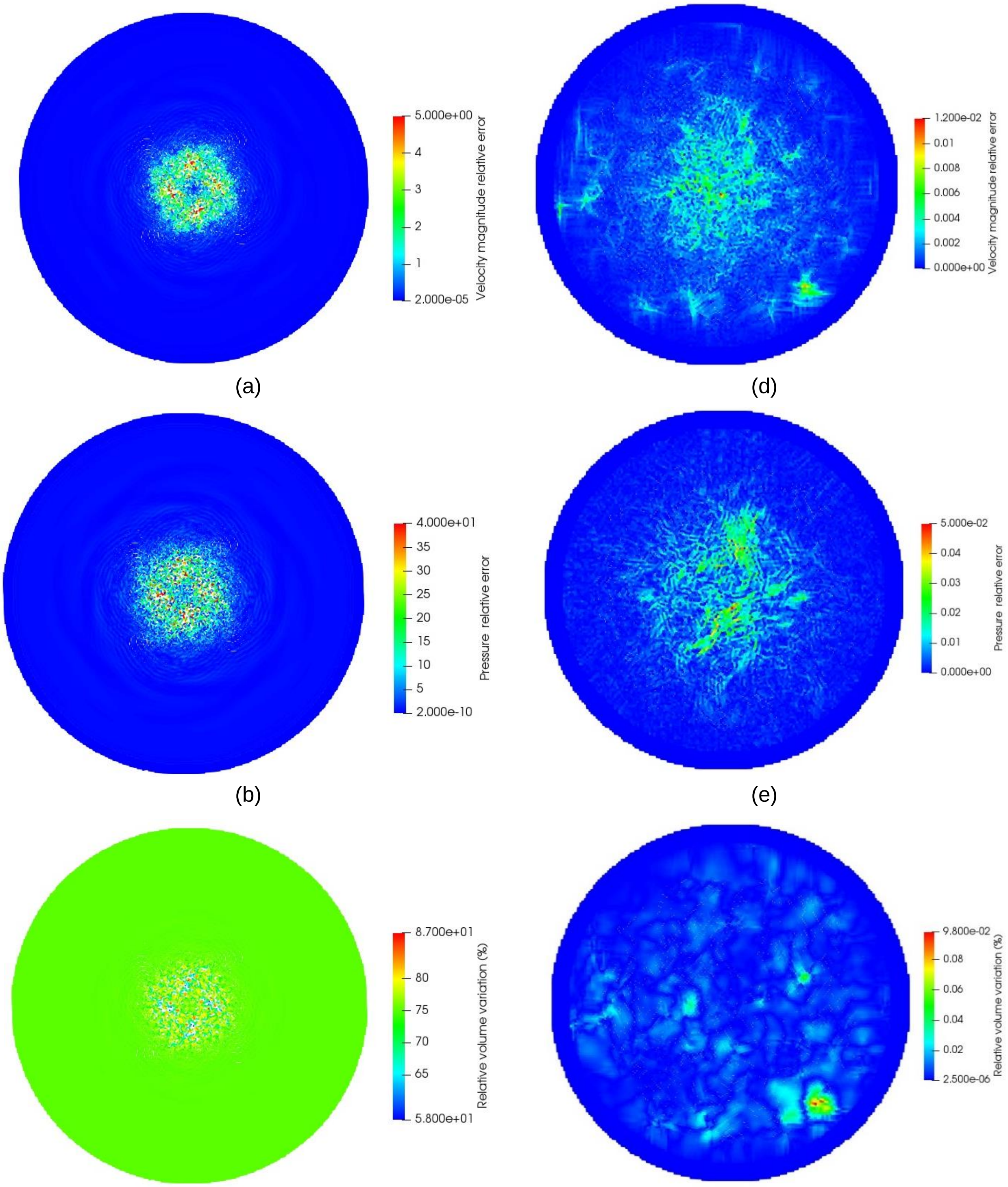

(a) (d)

(b) (e)

(c) (f)

Figure 24: Inviscid vortex relative error in (a, e) velocity magnitude (b. f) the pressure and (c, f) the volume at t = 2.2 sec with particle resolution of dx = 0.01 using the Wendland kernel with the ALE scheme with one shifting iteration (left) and the proposed ALE-IS scheme (right)

To evaluate the error and convergence characteristics of the ALE-IS scheme with arbitrary distributed particles, a spatial convergence study has been conducted.

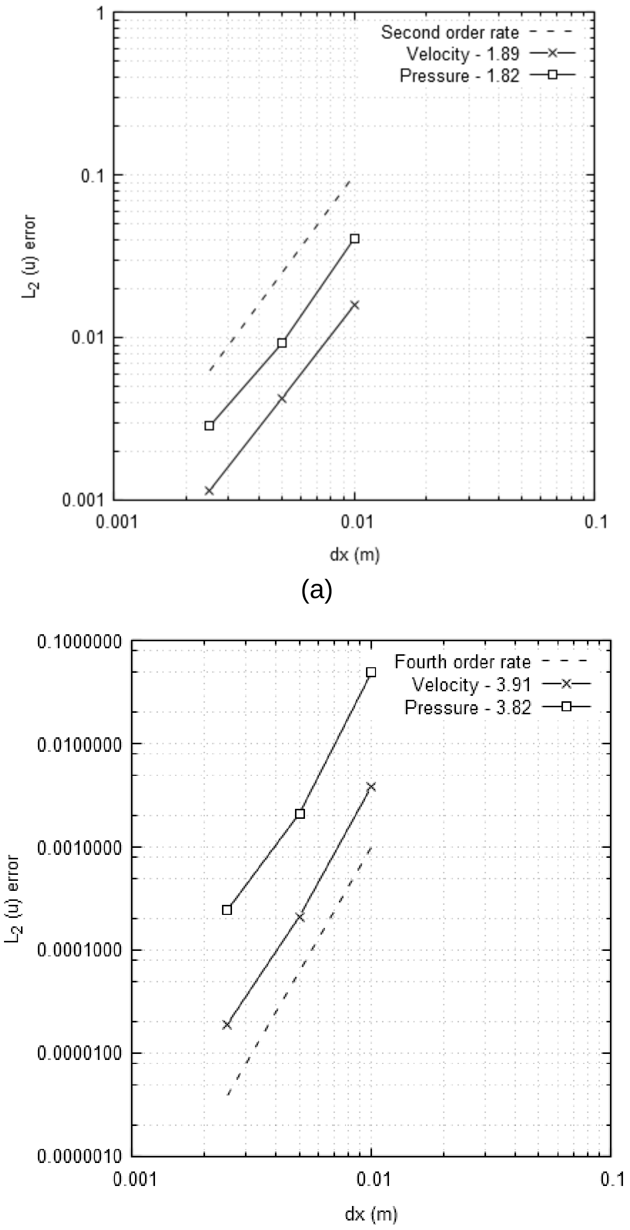

(a)

(b)

Figure 25: Spatial convergence rates for the bounded inviscid vortex using (a) the Wendland kernel and (b) the Gaussian G4 kernel

The velocity and pressure convergence rates is examined for two different kernels. Firstly, the Wendland kernel of Equation 33 is used with a theoretical rate of convergence of two and secondly the Gaussian G4 kernel of Equation 34 is used with a theoretical rate of convergence of four and a support radius of $4h$. As expected and demonstrated in Figure 22 for the Wendland kernel a rate of convergence of 1.9 is shown in Figure 25(a). Most importantly, the results for the Gaussian kernel are shown in Figure 25(b) with a convergence rate of 3.9 near the theoretical convergence of the 4th order accurate Gaussian kernel. The above convergence rates demonstrate the accuracy that can be achieved using the proposed ALE-IS scheme.

6 Conclusions

The incompressible Smoothed Particle Hydrodynamics (ISPH) scheme is known to have noise-free pressures and kinematics for internal and free-surface flows. However, the non-uniformity of particles restricts the accuracy and, consequently, the convergence of the solution to lower than the theoretical second-order convergence in smoothing length.

The recent developments of high-order incompressible SPH within an Eulerian framework of Lind and Stansby [6] removed the error associated with non-uniformity of particles, and demonstrated near ideal convergence characteristics. However, those improvements were only applicable to open periodic domains, and the particle distribution was restricted to a Cartesian arrangement only, so arbitrary geometries were not possible.

This novel and original research at the University of Manchester has extended the incompressible SPH scheme to bounded domains, so that it can be applied to arbitrary geometries, as well as multi-phase and multiple continua flows, through the following SPH developments:

- **Wall bounded arbitrary geometries:** An iterative particle shifting methodology applicable to the Eulerian SPH scheme has been developed where the iterative scheme is only applied once, in the beginning of the simulation as a pre-processing step. The iterative shifting scheme comprises a two-step shifting approach that minimise the particle shifting distance. A polynomial field function of the same order as the kernel with a tolerance over a regular distribution of 10% must also be satisfied before the iteration procedure is considered to have converged. The effectiveness of the iterative shifting scheme for arbitrary wall bounded domains has been demonstrated using a number of 3-D Poiseuille flow test cases in circular and non-circular cross-sections with close to second-order rate of convergence.
- **Higher-order boundary conditions:** A necessity for higher order convergence rates is the use of a higher order wall boundary condition. Therefore, a novel high-order accurate extrapolation technique for the enforcement of wall and open boundaries to high-order accuracy with Eulerian ISPH was developed and validated. Fourth-order convergence was demonstrated for the 3-D spiral annular flow field smoothing kernel interpolations and third-order spatial accuracy was demonstrated for full 3-D simulations of axial flow through a cylindrical annulus.
- **Arbitrary Lagrangian-Eulerian (ALE) formulation:** A consistent ALE SPH scheme was developed in order to attain the Lagrangian characteristics of SPH to make it applicable to multi-phase flows. This ensures near isotropic particle spacing and therefore, near to theoretical convergence rates without an instability developing due to mass flux from the ALE formulation with no corrections needed to increase the accuracy of the SPH discrete operators. The scheme has been validated for unbounded and bounded domains using the Taylor-Green vortices and inviscid vortex test cases, and shows large improvements in accuracy and stability compared to other ALE schemes. A spatial convergence study has also been performed where second- and fourth-order convergence rates have been demonstrated. These developments are directly applicable to, and have been developed to accommodate, interfacial boiling flows.

These innovative SPH developments in terms of accuracy, convergence rates and arbitrary geometries mean that this meshless method could be applied to nuclear thermal hydraulics in realistic geometries. This has the potential to reduce the time and cost associated with nuclear thermal hydraulic analyses in the future.

7 References

[1] Bate, M.R. and A. Burkert, *Resolution Requirements for Smoothed Particle Hydrodynamics Calculations with Self-Gravity.* Monthly Notices of the Royal Astronomical Society, 1997. **288**(4): p. 1060-1072.

[2] Crespo, A.J., et al., *Dualsphysics: Open-Source Parallel Cfd Solver Based on Smoothed Particle Hydrodynamics (Sph).* Computer Physics Communications, 2015. **187**: p. 204-216.

[3] Fourtakas, G., *Modelling Multi-Phase Flows in Nuclear Decommissioning Using Sph*. 2014, University of Manchester.

[4] Leroy, A., et al., *Buoyancy Modelling with Incompressible Sph for Laminar and Turbulent Flows.* International Journal for Numerical Methods in Fluids, 2015. **78**(8): p. 455-474.

[5] Mayrhofer, A., et al., *Dns and Les of 3-D Wall-Bounded Turbulence Using Smoothed Particle Hydrodynamics.* Computers & Fluids, 2015. **115**: p. 86-97.

[6] Lind, S. and P. Stansby, *High-Order Eulerian Incompressible Smoothed Particle Hydrodynamics with Transition to Lagrangian Free-Surface Motion.* Journal of Computational Physics, 2016. **326**: p. 290-311.

[7] Xu, R., P. Stansby, and D. Laurence, *Accuracy and Stability in Incompressible Sph (Isph) Based on the Projection Method and a New Approach.* Journal of Computational Physics, 2009. **228**(18): p. 6703-6725.

[8] Morris, J.P., P.J. Fox, and Y. Zhu, *Modeling Low Reynolds Number Incompressible Flows Using Sph.* Journal of computational physics, 1997. **136**(1): p. 214-226.

[9] Monaghan, J.J., *Smoothed Particle Hydrodynamics.* Annual review of astronomy and astrophysics, 1992. **30**(1): p. 543-574.

[10] Cummins, S.J. and M. Rudman, *An Sph Projection Method.* Journal of Computational Physics, 1999. **152**(2): p. 584-607.

[11] Quinlan, N.J., M. Basa, and M. Lastiwka, *Truncation Error in Mesh-Free Particle Methods.* International Journal for Numerical Methods in Engineering, 2006. **66**(13): p. 2064-2085.

[12] Monaghan, J., *On the Problem of Penetration in Particle Methods.* Journal of Computational physics, 1989. **82**(1): p. 1-15.

[13] Lind, S., et al., *Incompressible Smoothed Particle Hydrodynamics for Free-Surface Flows: A Generalised Diffusion-Based Algorithm for Stability and Validations for Impulsive Flows and Propagating Waves.* Journal of Computational Physics, 2012. **231**(4): p. 1499-1523.

[14] Khayyer, A., H. Gotoh, and Y. Shimizu, *Comparative Study on Accuracy and Conservation Properties of Two Particle Regularization Schemes and Proposal of an Optimized Particle Shifting Scheme in Isph Context.* Journal of Computational Physics, 2017. **332**: p. 236-256.

[15] Oger, G., et al., *Sph Accuracy Improvement through the Combination of a Quasi-Lagrangian Shifting Transport Velocity and Consistent Ale Formalisms.* Journal of Computational Physics, 2016. **313**: p. 76-98.

[16] Hu, X. and N. Adams, *A Constant-Density Approach for Incompressible Multi-Phase Sph.* Journal of Computational Physics, 2009. **228**(6): p. 2082-2091.

[17] Chaniotis, A., D. Poulikakos, and P. Koumoutsakos, *Remeshed Smoothed Particle Hydrodynamics for the Simulation of Viscous and Heat Conducting Flows.* Journal of Computational Physics, 2002. **182**(1): p. 67-90.

[18] Vacondio, R. and B.D. Rogers, *Consistent Iterative Shifting for Sph Methods*, in *Proceedings of the 12th International SPHERIC Workshop*, A.J.C. Crespo, Editor. 2017: Ourense, Spain.

[19] Adami, S., X. Hu, and N. Adams, *A Generalized Wall Boundary Condition for Smoothed Particle Hydrodynamics.* Journal of Computational Physics, 2012. **231**(21): p. 7057-7075.

[20] Monaghan, J.J., *Sph without a Tensile Instability.* Journal of Computational Physics, 2000. **159**(2): p. 290-311.

[21] Swegle, J., D. Hicks, and S. Attaway, *Smoothed Particle Hydrodynamics Stability Analysis.* Journal of computational physics, 1995. **116**(1): p. 123-134.

[22] Liu, M., G. Liu, and K. Lam, *Constructing Smoothing Functions in Smoothed Particle Hydrodynamics with Applications.* Journal of Computational and applied Mathematics, 2003. **155**(2): p. 263-284.

[23] Guo, X., et al., *New Massively Parallel Scheme for Incompressible Smoothed Particle Hydrodynamics (Isph) for Highly Nonlinear and Distorted Flows.* under review.

[24] Bazant, M.Z., *Exact Solutions and Physical Analogies for Unidirectional Flows.* Physical Review Fluids, 2016. **1**(2): p. 024001.

[25] Fourtakas, G., et al., *Local Uniform Stencil (Lust) Boundary Conditions for 3-D Irregular Boundaries in Dualsphysics*, in *9th SPHERIC Workshop*. 2014: Paris, France.

[26] Monaghan, J.J., *Simulating Free Surface Flows with Sph.* Journal of computational physics, 1994. **110**(2): p. 399-406.

[27] Ferrand, M., et al., *Unified Semi-Analytical Wall Boundary Conditions for Inviscid, Laminar or Turbulent Flows in the Meshless Sph Method.* International Journal for Numerical Methods in Fluids, 2013. **71**(4): p. 446-472.

[28] Takeda, H., S.M. Miyama, and M. Sekiya, *Numerical Simulation of Viscous Flow by Smoothed Particle Hydrodynamics.* Progress of Theoretical Physics, 1994. **92**(5): p. 939-960.

[29] Xu, R., P.K. Stansby, and D.R. Laurence, *Accuracy and Stability in Incompressible Sph (Isph) Based on the Projection Method and a New Approach.* Journal of Computational Physics, 2009. **228**(18): p. 6703-6725.

[30] Xenakis, A., et al., *An Incompressible Sph Scheme with Improved Pressure Predictions for Free-Surface Generalised Newtonian Flows.* Journal of Non-Newtonian Fluid Mechanics, 2015. **218**: p. 1-15.

[31] Nasar, A.M.A., *Eulerian and Lagrangian Smoothed Particle Hydrodynamics as Models for the Interaction of Fluids and Flexible Structures in Biomedical Flows.* Ph. D. Thesis, The University of Manchester, UK, 2016.

[32] Monaghan, J., *Extrapolating B Splines for Interpolation.* Journal of Computational Physics, 1985. **60**(2): p. 253-262.

[33] Chaniotis, A. and D. Poulikakos, *High Order Interpolation and Differentiation Using B-Splines.* Journal of Computational Physics, 2004. **197**(1): p. 253-274.

[34] Wendland, H., *Piecewise Polynomial, Positive Definite and Compactly Supported Radial Functions of Minimal Degree.* Advances in computational Mathematics, 1995. **4**(1): p. 389-396.

[35] Bonet, J. and T.-S. Lok, *Variational and Momentum Preservation Aspects of Smooth Particle Hydrodynamic Formulations.* Computer Methods in applied mechanics and engineering, 1999. **180**(1): p. 97-115.

[36] Colagrossi, A. and M. Landrini, *Numerical Simulation of Interfacial Flows by Smoothed Particle Hydrodynamics.* Journal of computational physics, 2003. **191**(2): p. 448-475.

[37] Lind, S., et al., *Incompressible Smoothed Particle Hydrodynamics for Free-Surface Flows: A Generalised Diffusion-Based Algorithm for Stability and Validations for Impulsive Flows and Propagating Waves.* Journal of Computational Physics, 2012. **231**(4): p. 1499-1523.

[38] Bonet, J. and T.-S. Lok, *Variational and Momentum Preservation Aspects of Smooth Particle Hydrodynamic Formulations.* Computer Methods in applied mechanics and engineering, 1999. **180**(1-2): p. 97-115.

[39] Litvinov, S., X. Hu, and N.A. Adams, *Towards Consistence and Convergence of Conservative Sph Approximations.* Journal of Computational Physics, 2015. **301**: p. 394-401.

[40] Monaghan, J.J., M.C. Thompson, and K. Hourigan, *Simulation of Free Surface Flows with Sph.* 1994.

[41] Skillen, A., et al., *Incompressible Smoothed Particle Hydrodynamics (Sph) with Reduced Temporal Noise and Generalised Fickian Smoothing Applied to Body–Water Slam and Efficient Wave–Body Interaction.* Computer Methods in Applied Mechanics and Engineering, 2013. **265**: p. 163-173.

[42] Vacondio, R., et al., *Variable Resolution for Sph: A Dynamic Particle Coalescing and Splitting Scheme.* Computer Methods in Applied Mechanics and Engineering, 2013. **256**: p. 132-148.

[43] Mokos, A., B.D. Rogers, and P.K. Stansby, *A Multi-Phase Particle Shifting Algorithm for Sph Simulations of Violent Hydrodynamics with a Large Number of Particles.* Journal of Hydraulic Research, 2017. **55**(2): p. 143-162.

[44] Fourtakas, G. and B. Rogers, *Modelling Multi-Phase Liquid-Sediment Scour and Resuspension Induced by Rapid Flows Using Smoothed Particle Hydrodynamics (Sph) Accelerated with a Graphics Processing Unit (Gpu).* Advances in water resources, 2016. **92**: p. 186-199.

[45] Sun, P., et al., *The Δplus-Sph Model: Simple Procedures for a Further Improvement of the Sph Scheme.* Computer Methods in Applied Mechanics and Engineering, 2017. **315**: p. 25-49.

[46] Sun, P., et al., *A Consistent Approach to Particle Shifting in the Δ-Plus-Sph Model.* Computer Methods in Applied Mechanics and Engineering, 2019. **348**: p. 912-934.

[47] Vila, J., *On Particle Weighted Methods and Smooth Particle Hydrodynamics.* Mathematical models and methods in applied sciences, 1999. **9**(02): p. 161-209.

[48] Colagrossi, A., et al., *Notes on the Sph Model within the Arbitrary-Lagragian-Eulerian Framework*, in *13th international SPHERIC workshop*, N.J. Quinlan, Editor. 2018: Galway, Ireland.

[49] Michel, J., G. Oger, and D. Le Touzé, *Effects of Particle Disordering on Local and Global Fluid Volume in the Sph Method and Proposition of an Improved Sph-Ale Scheme*, in *13th international SPHERIC workshop*, N.J. Quinlan, Editor. 2018: Galway, Ireland.

[50] Vacondio, R. and B.D. Rogers, *Consistent Iterative Shifting for Sph Methods*, in *12th international SPHERIC workshop*, A. Crsepo, Editor. 2017: Ourense, Spain.

[51] Belytschko, T., et al., *Nonlinear Finite Elements for Continua and Structures*. 2013: John wiley & sons.

[52] Monaghan, J.J., *Smoothed Particle Hydrodynamics.* Reports on progress in physics, 2005. **68**(8): p. 1703.

[53] Monaghan, J. and A. Kos, *Solitary Waves on a Cretan Beach.* Journal of waterway, port, coastal, and ocean engineering, 1999. **125**(3): p. 145-155.

[54] Monaghan, J., *On the Problem of Penetration in Particle Methods.* Journal of Computational physics, 1989. **82**: p. 1-15.

[55] Fourtakas, G., et al., *Towards High-Order 3-D Eulerian Incompressible Sph for Arbitrary Geometries with Generalised Particle Distributions*, in *13th SPHERIC International Workshop*, N.J. Quinlan, Editor. 2018: Galway, Ireland.

[56] Fourtakas, G., et al., *An Eulerian–Lagrangian Incompressible Sph Formulation (Eli-Sph) Connected with a Sharp Interface.* Computer Methods in Applied Mechanics and Engineering, 2018. **329**: p. 532-552.

DOCUMENT INFORMATION

Project :	Project FORTE - Nuclear Thermal Hydraulics Research & Development
Report Title :	Incompressible SPH for Arbitrary Wall Bounded Geometries
Client :	Department for Business, Energy and Industrial Strategy (BEIS)

Report No. :	FNC 53798/48656R	**Compiled By :**	Dr G. Fourtakas (The University of Manchester)
Issue No. :	1	**Verified By :**	Prof P. Stansby (The University of Manchester)
Date :	August 2019	**Approved By :**	R. Underhill

Legal Statement

This document has been prepared for the UK Government Department for Business, Energy and Industrial Strategy (BEIS) by Frazer-Nash Consultancy Ltd, and any statements contained herein referring to ‘we’ or ‘our’ shall apply to Frazer-Nash Consultancy and BEIS both individually and jointly.

The Copyright in this work is vested in Frazer-Nash Consultancy Limited. Reproduction in whole or in part or use for tendering or manufacturing purposes is prohibited except under an agreement with or with the written consent of Frazer-Nash Consultancy Limited and then only on the condition that this notice is included in any such reproduction.

This document is provided for general information only. It is not intended to amount to advice or suggestions on which any party should, or can, rely. You must obtain professional or specialist advice before taking or refraining from taking any action on the basis of the content of this document.

We make no representations and give no warranties or guarantees, whether express or implied, that the content of this document is accurate, complete, up to date, free from any third party encumbrances or fit for any particular purpose. We disclaim to the maximum extent permissible and accept no responsibility for the consequences of this document being relied upon by you, any other party or parties, or being used for any purpose, or containing any error or omission.

Except for death or personal injury caused by our negligence or any other liability which may not be excluded by an applicable law, we will not be liable to any party placing any form of reliance on the document for any loss or damage, whether in contract, tort (including negligence) breach of statutory duty, or otherwise, even if foreseeable, arising under or in connection with use of or reliance on any content of this document in whole or in part.

This document represents the views of Frazer-Nash Consultancy Limited and does not represent the views of BEIS or the UK Government more widely.

Originating Office: FRAZER-NASH CONSULTANCY LIMITED
The Cube, 1 Lower Lamb Street, Bristol, BS1 5UD
T: +44 (0)117 9226242   F: +44 (0)117 9468924   W: www.fnc.co.uk

Frazer-Nash Consultancy Ltd
The Cube
1 Lower Lamb Street
Bristol
BS1 5UD

T +44 (0)117 9226242
F +44 (0)117 9468924

www.fnc.co.uk

Offices at:
Bristol, Burton-on-Trent, Dorchester,
Dorking, Glasgow, Plymouth, Warrington
and Adelaide